British Antarctic Survey's Aerogeophysical Data: Releasing 25 Years of Airborne Gravity, Magnetic, and Radar Datasets over Antarctica

Alice C. Frémand[1*], Julien A. Bodart[1, 2*], Tom A. Jordan[1], Fausto Ferraccioli[1, 3], Carl Robinson[1], Hugh F.J. Corr[1], Helen J. Peat[1], Robert G. Bingham[2], and David G. Vaughan[1]

[1] British Antarctic Survey, Cambridge, UK.
[2] School of GeoSciences, University of Edinburgh, Edinburgh, UK.
[3] Istituto Nazionale di Oceanografia e di Geofisica Sperimentale, Trieste, Italy

* These authors contributed equally to this work.

Corresponding authors: Alice C. Fremand (almand@bas.ac.uk) and Julien A. Bodart (julien.bodart@ed.ac.uk)

Key Points

- We present the release of 64 aerogeophysical datasets (including gravity, magnetic, bed-pick, and radar data) obtained from 24 surveys flown by the British Antarctic Survey over West Antarctica, East Antarctica, and the Antarctic Peninsula between 1994 and 2020.

- The published datasets have been standardised according to the FAIR (Findable, Accessible, Interoperable and Re-Usable) data principles and integrated into a user-friendly data interface, the Polar Airborne Geophysics Data Portal, to further enhance the interactivity of the datasets.

- We discuss how the data were acquired and processed and show the potential re-usability of the newly released aerogeophysical data by investigating the englacial architecture of the ice from airborne radars using an automatic layer-continuity method.

Abstract

Over the past 50 years, the British Antarctic Survey (BAS) has been one of the major acquirers of aerogeophysical data over Antarctica, providing scientists with gravity, magnetic and radar datasets that have been central to many studies of the past, present, and future evolution of the Antarctic Ice Sheet. Until recently, many of these datasets were not openly available, restricting further usage of the data for different glaciological and geophysical applications. Starting in 2020, scientists and data managers at BAS have worked on standardising and releasing large swaths of aerogeophysical data acquired during the period 1994-2020, including a total of 64 datasets from 24 different surveys, amounting to ~450,000 line-km (or 5.3 million km^2) of data across West Antarctica, East Antarctica, and the Antarctic Peninsula. Amongst these are the extensive surveys over the fast-changing Pine Island (BBAS 2004-05) and Thwaites (ITGC 2018-19 & 2019-20) glacier catchments, and the first ever surveys of the Wilkes Subglacial Basin (WISE-ISODYN 2005-06) and Gamburtsev Subglacial Mountains (AGAP 2007-09). Considerable effort has been made to standardise these datasets to comply with the FAIR (Findable, Accessible, Interoperable and Re-Usable) data principles, as well as to create the Polar Airborne Geophysics Data Portal (https://www.bas.ac.uk/project/nagdp/), which serves as a user-friendly interface to interact with and download the newly published data. This paper reviews how these datasets were acquired and processed, presents the methods used to standardise them, and introduces the new data portal and interactive tutorials that were created to improve the accessibility of the data. Lastly, we exemplify future potential uses of the aerogeophysical datasets by extracting information on the continuity of englacial layering from the fully published airborne radar data. We believe this newly released data will be a valuable asset to future glaciological and geophysical studies over Antarctica and will extend significantly the life cycle of the data. All datasets included in this data release are now fully accessible at: https://data.bas.ac.uk.

Key Words: Aerogeophysics, Gravity, Magnetics, Radar, Antarctica, Airborne, Ice Thickness, Data, FAIR

1. Introduction

As one of the fastest changing environments on Earth, Antarctica has been at the epicentre of scientific research since the early 1960s. Understanding the past, present, and future of the Antarctic Ice Sheet is of special interest, particularly in the context of rapid climatic changes already affecting large parts of the Antarctic Peninsula and threatening the stability of the West Antarctic Ice Sheet (IPCC, 2021). One way to quantify how the ice sheet will respond to these changes is to conduct studies of englacial and basal properties of the ice using geophysical techniques such as gravity, magnetic, and radar. By studying the bedrock topography beneath an ice sheet, we can better estimate where a retreating ice stream is more likely to stabilise or de-stabilise further (Holt et al., 2006; Vaughan et al., 2006; Tinto and Bell, 2011; Ross et al., 2012; Morlighem et al., 2020) and how landforms or subglacial water-routing systems can affect the flow-regime of ice streams (Bell et al., 2011; Wright et al., 2012; Schroeder et al., 2013; Ashmore and Bingham, 2014; Siegert et al., 2014; Young et al., 2016; Napoleoni et al., 2020). By studying the subglacial geology, we can better understand magmatic, tectonic and sedimentary influences on ice flow over timescales of hundreds, thousands or even millions of years (Bell et al., 1998; Blankenship et al., 2001; Studinger et al., 2001; Bamber et al., 2006; Bell et al., 2006; Jordan et al., 2010; Bingham et al., 2012), and quantify the influence of geothermal heat flux on ice dynamics (Schroeder et al., 2014; Jordan et al., 2018). Finally, the use of gravity techniques enables us to better understand the bathymetry beneath fast-changing ice shelves and ice-stream fronts and quantify areas of high sensitivity (Greenbaum et al., 2015; Millan et al., 2017; Tinto et al., 2019; Jordan et al., 2020).

Since the mid-1960s, the British Antarctic Survey (BAS) has been involved in acquiring aerogeophysical data with a particular focus on radar-data acquisition using a 35- and 60-MHz radio-echo sounder developed at the Scott Polar Research Institute (Robin et al., 1970), and, in collaboration with the Technical University of Denmark, using slightly improved versions of the same analogue radar system until the early 1990s (Robin et al., 1977). The subsequent development of an in-house digital radar system at BAS in 1993-94 (Corr and Popple, 1994), and accompanying gravity and magnetic instruments, allowed for the first surveys over West Antarctica's Evans Ice Stream to be conducted in 1994-95, marking the start of modern digital aerogeophysical surveying of the Antarctic by BAS. Further improvements in survey techniques and instruments have allowed BAS to develop its aerogeophysical capabilities further and become one of the leaders in aerogeophysics over the Antarctic.

Since the mid-1990s, aerogeophysical datasets acquired by BAS have played a vital role in understanding past and current ice-dynamical and lithospheric processes over the Antarctic Ice Sheet. In total, BAS flew 24 survey campaigns between 1994 and 2020, representing a total of ~450,000 line-km of aerogeophysical data over the Antarctic Peninsula and the West and East Antarctic Ice Sheets (hereafter abbreviated to WAIS and EAIS, respectively) (Fig. 1, Table 1). The total cumulative survey coverage since 1994 is 5.3 million km^2, equivalent to > 30 % of the total area of the Antarctic Ice Sheet (14.2 million km^2). Many of these surveys were acquired as part of large international collaborative projects such as the International Polar Year AGAP project, the European Space Agency (ESA) PolarGAP project, and the US-UK International Thwaites Glacier Collaboration (ITGC), amongst others. Importantly, much of the data acquired since then have been central to the output of large international science groups, such as the SCAR-funded (Scientific Committee on Antarctic Research) BEDMAP (I/II/III), ADMAP (I/II), AntArchitecture, and IBCSO projects (Lythe et al., 2001; Arndt et al., 2013; Fretwell et al., 2013; Golynsky et al., 2018).

104
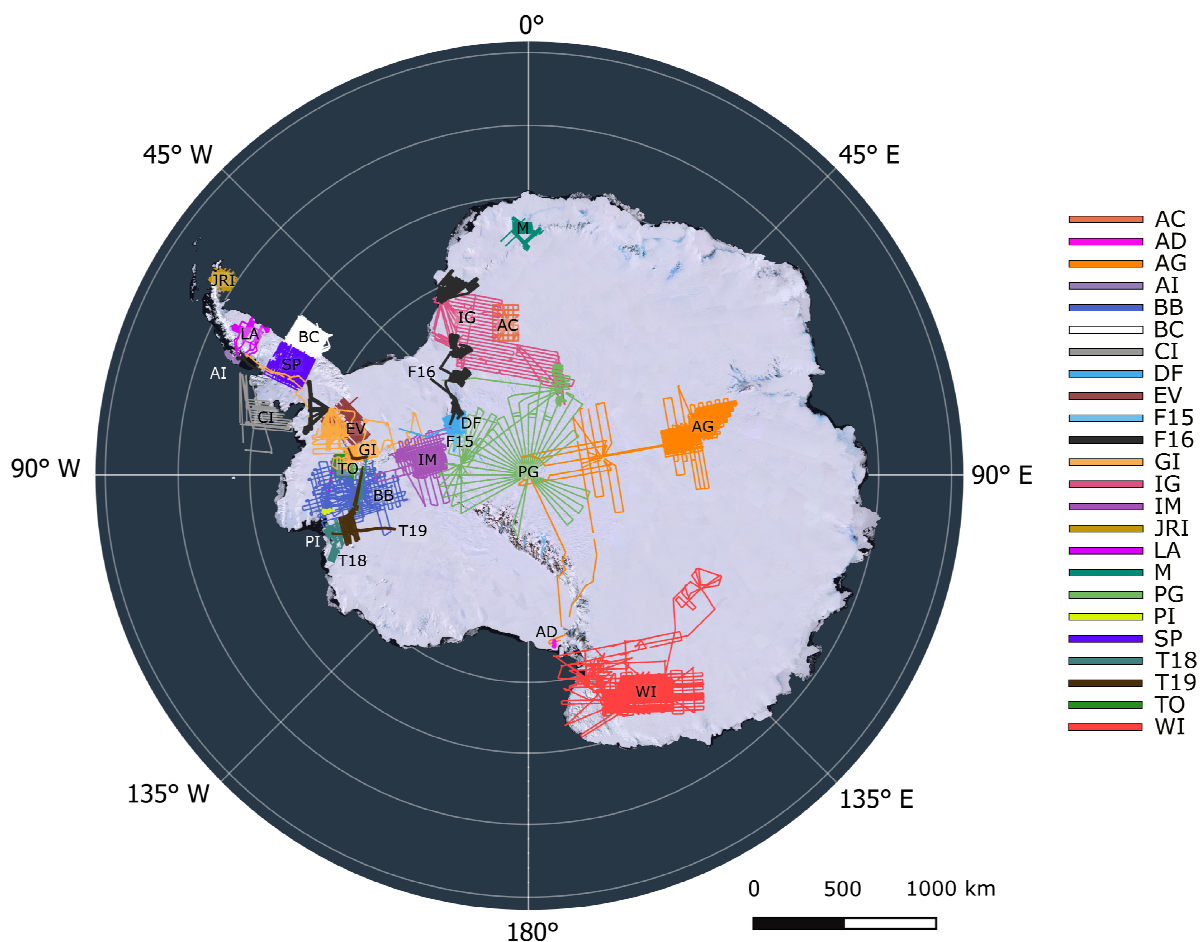
Figure 1. Map showing all the published datasets included in this data release. The colours are the same as those used on the data portal interface. Abbreviations are as follows: AC: AFI Coats Land (2001-02); AD: Andrill HRAM (2008-09); AG: AGAP (2007-09); AI: Adelaide Island (2010-11); BB: BBAS (2004-05); BC: Black Coast (1996-97); CI: Charcot Island (1996-97); DF: DUFEK (1998-99); EV: EVANS (1994-95); F15: FISS 2015 (2015-16); F16: FISS-EC-Halley 2016 (2015-16); GI: GRADES-IMAGE (2006-07); IG: ICEGRAV (2012-13); IM: IMAFI (2010-11); JRI: James Ross Island (1997-98); LA: Larsen Ice Shelf (1997-98); M: MAMOG (2001-02); PG: PolarGAP (2015-16); PI: Pine Island Glacier Ice Shelf (2010-11); SP: SPARC (2002-03); T18: ITGC Thwaites (2018-19); T19: ITGC Thwaites (2019-20); TO: TORUS (2001-02); WI: WISE-ISODYN (2005-06). The legend on the right-hand side of the figure shows the colour corresponding to each survey. The background image is from the Landsat Image Mosaic of Antarctica (LIMA; Bindschadler et al., 2008).

Despite the importance of these surveys for understanding the Antarctic cryosphere and tectonics, until now the underlying data have been relatively inaccessible to the wider scientific communities due to the scale of the data-management task required. This lack of accessibility has hampered the ability of the wider research community to extract further valuable information from these datasets. In 2020, a collaborative project between the UK Polar Data Centre (PDC, https://www.bas.ac.uk/data/uk-pdc/) and the BAS Airborne Geophysics science team was set up to improve the FAIR-ness (Findability, Accessibility, Interoperability and Re-Usability; Wilkinson et al., 2016) of these data. The main objectives of this collaboration were to comply with national and international policies on data sharing and accessibility, foster new collaborations, and allow the further re-use of these data beyond the lifespan of the science projects.

This paper presents the result of this successful collaboration between data managers and scientists to standardise and release most of BAS' aerogeophysical data acquired to date using modern

128   instruments from 1994 onwards. Data acquired prior to this, while particularly useful to long-term
129   monitoring of ice sheet conditions, are much more challenging and time-consuming to bring up to
130   modern standards (see Schroeder et al., 2019; Sect 5.3), and are thus not included in the data release
131   discussed here. Section 2 of this paper reviews the main scientific findings from each survey flown
132   between 1994 and 2020. Section 3 describes the various instruments and techniques used to acquire
133   and process the data. Section 4 outlines the format and data publishing strategy for our datasets
134   following the FAIR data principles, as well as the creation of a new data portal and interactive, open-
135   access tutorials. Finally, Section 5 provides a case study for the re-usability of the newly released
136   aerogeophysical data, as well as suggestions on future uses of the data portal and aspirations for future
137   data releases.

138

2. Background

140   The following section reviews the main scientific findings related to the acquisition of
141   aerogeophysical data from BAS for the period 1994-2020 and is divided into two sub-sections:
142   findings from surveys conducted pre-2004 using older aerogeophysical instruments and for which the
143   fully processed 2-D radar data is not published as part of this data release (see Table 1, Section 5.3),
144   and surveys conducted post-2004 using the PASIN-1 (2004-2015) and PASIN-2 (2015-2020) radar
145   systems and more modern data acquisition methods. Figures 2-3 present the wide-ranging datasets of
146   gravity and magnetic anomalies, bed elevation and ice thickness, and 2-D radar profiles ensuing from
147   the surveys discussed in sections 2.1. and 2.2.

2.1. Aerogeophysical Surveys for the Period 1994-2004

149   The first surveys conducted by BAS since the mid-1990s involved extensive gravity and
150   magnetic surveying of the western and eastern Antarctic Peninsula and Weddell Sea Embayment.
151   Surveys over Evans Ice Stream (1994-95), Black Coast (1996-97), Charcot Island (1996-97), and
152   James Ross Island (1997-98) (Fig. 1, Table 1) provided new insights into the history of crustal
153   boundaries between the eastern Antarctic Peninsula and the Filchner Block (Ferris et al., 2002),
154   evidence of crustal thinning below Evans Ice Stream (Jones et al., 2002), and new understanding of
155   the magmatic and tectonic processes around the Mount Haddington stratovolcano on James Ross
156   Island (Jordan et al., 2009). A further study covering the Larsen Ice Shelf (Antarctic Peninsula) was
157   conducted conjointly by BAS and Instituto Antártico Argentino in 1997-98. The radar data acquired
158   during this survey was used in ocean (Holland et al., 2009) and firn-density (Holland et al., 2011)
159   models to improve our understanding of ice-ocean interactions and ice-surface elevation change on
160   the ice shelf. In 1998-99, extensive aeromagnetic surveying of the Dufek Massif (West Antarctica /
161   East Antarctica) revealed the presence of a Jurassic dyke swarm that likely acted as a magma
162   transport and feeder system to the Ferrar Large Igneous Province (Ferris et al., 2003). In 2001-02, an
163   additional survey was flown as part of the TORUS (Targeting ice-stream Onset Regions and Under-
164   ice Systems) initiative to assess the factors controlling the dynamics of the Rutford Ice Stream using
165   gravity, magnetic and radar instruments over a high-resolution grid spacing of ~10 km (Vaughan et
166   al., 2008). Lastly for the WAIS, the SPARC (Superterranes of the Pacific Margin Arc) campaign of
167   2002-03 over Northern Palmer Land (Antarctic Peninsula) used gravity and magnetic instruments to
168   reveal subglacial imprints of crustal growth linked with the Gondwana margin (Ferraccioli et al.,
169   2006).

170   Over East Antarctica, two surveys conducted in 2001-02 acquired detailed gravity, magnetic
171   and radar measurements over Slessor Glacier (AFI; Antarctic Funding Initiative Coats Land survey)
172   and Jutulstraumen Ice Stream (MAMOG; Magmatism as a Monitor of Gondwana break-up). The AFI
173   Coats Land survey, a UK initiative between BAS and the University of Bristol, provided the first
174   accurate measurements of ice thickness and bed elevation in the area (Rippin et al., 2003a) (Fig. 2),

175 and led to the discovery of a ~3-km thick sedimentary basin associated with a weak till layer at the
176 bed which enhances basal motion and affects the flow regime of this part of the EAIS (Rippin et al.,
177 2003a ; Bamber et al., 2006; Shepherd et al., 2006). The MAMOG survey revealed the presence of a
178 subglacial Jurassic continental rift in the area of western Dronning Maud Land, providing early
179 evidence for the initial Gondwana break up (Ferraccioli et al., 2005a; 2005b).

2.2. Aerogeophysical Surveys for the Period 2004-2020

181 Building from the surveys prior to 2004 which were relatively small in areal extent, BAS
182 began surveying larger areas from the mid-2000s onwards (Table 1), primarily due to enhanced
183 international collaborations and improvements in data acquisition and instruments which led to data
184 being acquired both at higher resolution and over larger spatial scales. The acquisition strategy was to
185 collect data from multiple geophysical sensors mounted on BAS' Twin Otter aircraft across every
186 survey, giving a holistic view of vast and previously unsurveyed regions (Fig. 4-5). The core sensor
187 suite included gravity and magnetic instruments used to understand the geological nature of the
188 subglacial basins and mountains along with their tectonic structure, alongside the radar system used to
189 map ice thickness and bed elevation. The development of a new radar system, the Polarimetric
190 Airborne System Instrument (PASIN) (PASIN-1, 2004-2015) (see Section 3.1.3), and an improved
191 version of the same system (PASIN-2, 2015-16 onwards), allowed for the efficient collection of high-
192 quality digital radar data for BAS-led campaigns in the Antarctic.

193 We describe the findings from these surveys into two sub-sections (Section 2.2.1 for surveys
194 between 2004-2015; Section 2.2.2 for surveys between 2015-20) to reflect the acquisition of data
195 prior to and following the upgrade of the PASIN system (see Section 3.1.3).

2.2.1 2004-2015

197 The first mission to utilise the PASIN-1 radar system was the 2004-05 BBAS survey of Pine
198 Island Glacier, which aimed to characterise the subglacial conditions of this sensitive glacier of West
199 Antarctica (Vaugan et al., 2006). This survey provided two key findings: a) the discovery of a deep
200 subglacial trough, 500 m at its deepest point and 250 km long, through which Pine Island Glacier
201 flows; and b) the existence of well-constrained valley walls which would likely provide a buffer
202 against a potential catastrophic collapse of the WAIS via Pine Island Glacier (Vaughan et al., 2006).
203 Further studies utilising this dataset focused primarily on bed characteristics and the subglacial
204 hydrology of the catchment (Rippin et al., 2011; Napoleoni et al., 2020; Chu et al., 2021), as well as
205 tracking englacial layers and quantifying past-accumulation rates (Corr and Vaughan, 2008; Karlsson
206 et al., 2009; 2014; Bodart et al., 2021). The survey was also conducted simultaneously with another
207 covering the Thwaites Glacier catchment led by the University of Texas Institute for Geophysics and
208 the National Science Foundation of the United States (Holt et al., 2006), enabling a comparison of the
209 surveying capabilities where the surveys overlapped (e.g. Chu et al., 2021).

210 **Table 1. Information on the period, region, sub-region, type of data acquired, total line-coverage**
211 **(km), total coverage area (km^2), and key reference for each survey included in this data release.** For
212 "Data", the abbreviations are as follows: Gravity (G), Magnetic (M), Radar (R). For "Regions", abbreviations
213 are as follows: APIS (Antarctic Peninsula Ice Sheet), EAIS (East Antarctic Ice Sheet), WAIS (West Antarctic
214 Ice Sheet). "DML" stands for Dronning Maud Land and "PIG" for Pine Island Glacier. The total area in km^2 is
215 calculated as a cumulative total area of the spatial footprint of the survey's minimum and maximum extent. *For
216 AGAP, the data release only consists of the BAS-acquired data, which represents approximately half of the total
217 (~120,000 km) survey coverage from the whole AGAP expedition (see Section 2.2.1).

Survey	Year	Region	Sub-Region	Data	Total line coverage (km)	Total coverage area (km^2)	Reference
EVANS	1994-95	WAIS/ APIS	Evans Ice Stream	G, M, R	11500	1.06×10^5	Jones et al. (2002)

Black Coast	1996-97	APIS	Black Coast/ Weddell Sea	M	10000	8.96×10^4	Ferris et al. (2002)
CHARCOT	1996-97	APIS	Charcot Island	M	7500	1.67×10^5	Johnson et al. (1999)
James Ross Island	1997-98	APIS	James Ross Island	G, M, R	10000	3.32×10^4	Jordan et al. (2009)
LARSEN	1997-98	APIS	Larsen Ice Shelf	M, R	5800	5.96×10^4	Holland et al. (2009)
DUFEK	1998-99	WAIS/ EAIS	Dufek Massif	G, M, R	8300	4.66×10^4	Ferris et al. (2003)
AFI Coats Land	2001-02	EAIS	Slessor Glacier	G, M, R	5000	6.53×10^4	Rippin et al. (2003a)
MAMOG	2001-02	EAIS	Jutulstraumen Ice Stream / DML	G, M, R	15500	5.79×10^4	Ferraccioli et al. (2005a)
TORUS	2001-02	WAIS	Rutford Ice Stream	G, M, R	8600	1.12×10^5	Vaughan et al. (2008)
SPARC	2002-03	APIS	Northern Palmer Land	G, M	20000	1.07×10^5	Ferraccioli et al. (2006)
BBAS	2004-05	WAIS	Pine Island Glacier	G, M, R	35000	4.09×10^5	Vaughan et al. (2006)
WISE-ISODYN	2005-06	EAIS	Wilkes Land	G, M, R	61000	7.91×10^5	Jordan et al. (2013)
GRADES-IMAGE	2006-07	WAIS/ APIS	Evans & Rutford ice streams	M, R	27500	3.06×10^5	Ashmore et al. (2014)
AGAP	2007-09	EAIS	Gamburtsev / Dome A	G, M, R	73000*	6.22×10^5	Ferraccioli et al. (2011)
ANDRILL HRAM	2008-09	WAIS	Ross Ice Shelf & Coulman High	M, R	1200	1.48×10^3	-
Adelaide Island	2010-11	APIS	Adelaide Island	M, R	5500	3.76×10^3	Jordan et al. (2014)
IMAFI	2010-11	WAIS	Institute & Möller ice streams	G, M, R	25000	1.96×10^5	Ross et al. (2012)
PIG Ice Shelf	2010-11	WAIS	Pine Island Shelf	M, R	1500	1.80×10^3	Vaughan et al. (2012)
ICEGRAV	2012-13	EAIS	Recovery & Slessor glaciers, Bailey Ice Stream	G, M, R	29000	4.75×10^5	Diez et al. (2018)
FISS 2015	2015-16	WAIS	Foundation Ice Stream / Bungenstock Ice Rise	M, R	7000	1.43×10^4	-
PolarGAP	2015-16	EAIS	South Pole	G, M, R	38000	8.71×10^5	Jordan et al. (2018)
FISS 2016	2016-17	WAIS	Filchner Ice Shelf / English Coast / Recovery & Support Force glaciers / Halley station	G, M, R	26000	5.99×10^5	Hofstede et al. (2021)
ITGC 2018	2018-20	WAIS	Thwaites Glacier	G, M, R	9872	6.43×10^4	Jordan et al. (2020)
ITGC 2019	2019-20	WAIS	Thwaites Glacier / WAIS Divide / Rutford Ice Stream	G, M, R	4432	4.85×10^4	-

218

219   Following on from the BBAS survey, the suite of geophysical instruments on board the BAS
220 Twin Otter aircraft were used to survey the Wilkes Subglacial Basin, Dome C, and the Transantarctic
221 Mountains as part of the 2005-06 WISE-ISODYN survey between BAS and the Italian Programma
222 Nazionale di Ricerche in Antartide (Bozzo and Ferraccioli, 2007; Corr et al., 2007; Ferraccioli et al.,
223 2007; Jordan et al., 2007). This project revealed, for the first time, the crustal architecture of the
224 Wilkes Subglacial Basin (Ferraccioli et al., 2009; Jordan et al., 2013) and the distribution of a well-
225 preserved subglacial sedimentary basin underlying the Wilkes catchment (Frederick et al., 2016). The
226 following year, the 2006-07 GRADES-IMAGE (Glacial Retreat in Antarctica and Deglaciation of the
227 Earth System - Inverse Modelling of Antarctica and Global Eustasy) survey, comprising surveys over
228 the transitional area between the Antarctic Peninsula and the WAIS, provided detailed information on
229 subglacial properties of Evans Ice Stream (Ashmore et al., 2014), ice-thickness measurements along
230 the grounding line were used as key calibration for the Landsat-derived "ASAID" grounding-line
231 product (Bindschadler et al., 2011), and englacial layers through Bungenstock Ice Rise were used to
232 assess ice-divide stability and the wider ice-flow history and stability of the WAIS's Weddell Sea
233 sector during the Holocene (Siegert et al., 2013).

234   Over two austral field seasons from 2007 to 2009, the AGAP (Antarctica's Gamburtsev
235 Province Project) survey, coordinated as part of the fourth International Polar Year between the UK,
236 USA, Germany, Japan, Australia and China, comprised a comprehensive survey of the interior of the
237 EAIS, yielding important aerogeophysical data used to interrogate the origin and geophysical
238 characteristics of the Gamburtsev Subglacial Mountains. Significant scientific discoveries generated
239 by the AGAP survey included observations of widespread freeze-on at the bottom of the ice which
240 leads to thickening of the EAIS from the base (Bell et al., 2011), a thick crustal root formed during the
241 Proterozoic aeon (1 Gyr ago) surrounded by a more recent ~2,500-km-long rift system (Ferraccioli et
242 al., 2011), and the existence of ancient pre-glacial fluvial networks at the present ice bed which
243 confirmed the presence of the Gamburtsev Subglacial Mountains prior to the start of glaciation at the
244 Eocene–Oligocene climate boundary (ca. 34 Ma) (Rose et al., 2013; Creyts et al., 2014).

245   Between 2008 and 2011, three surveys utilised the magnetic and radar instruments on board
246 the BAS Twin Otter to conduct high-spatial resolution surveying of Coulman High on Ross Ice Shelf
247 as part of the ANDRILL HRAM (Antarctic Drilling - High Resolution Aeromagnetic) project,
248 Adelaide Island (Antarctic Peninsula), and Pine Island Glacier Ice Shelf (West Antarctica). The 2010-
249 11 Adelaide Island survey provided high-resolution aeromagnetic data to underpin a better
250 understanding of the complex magmatic structure of the Antarctic Peninsula Cenozoic arc/forearc
251 boundary (Jordan et al., 2014). The Pine Island Glacier Ice Shelf survey of the same year revealed a
252 network of sinuous subglacial channels, 500- to 3000-m wide and up to 200-m high, in the ice-shelf
253 base, which, combined with surface and basal crevasses formed as a result of the basal melting, could
254 lead to structural weakening of the shelf in the future (Vaughan et al., 2012).

255
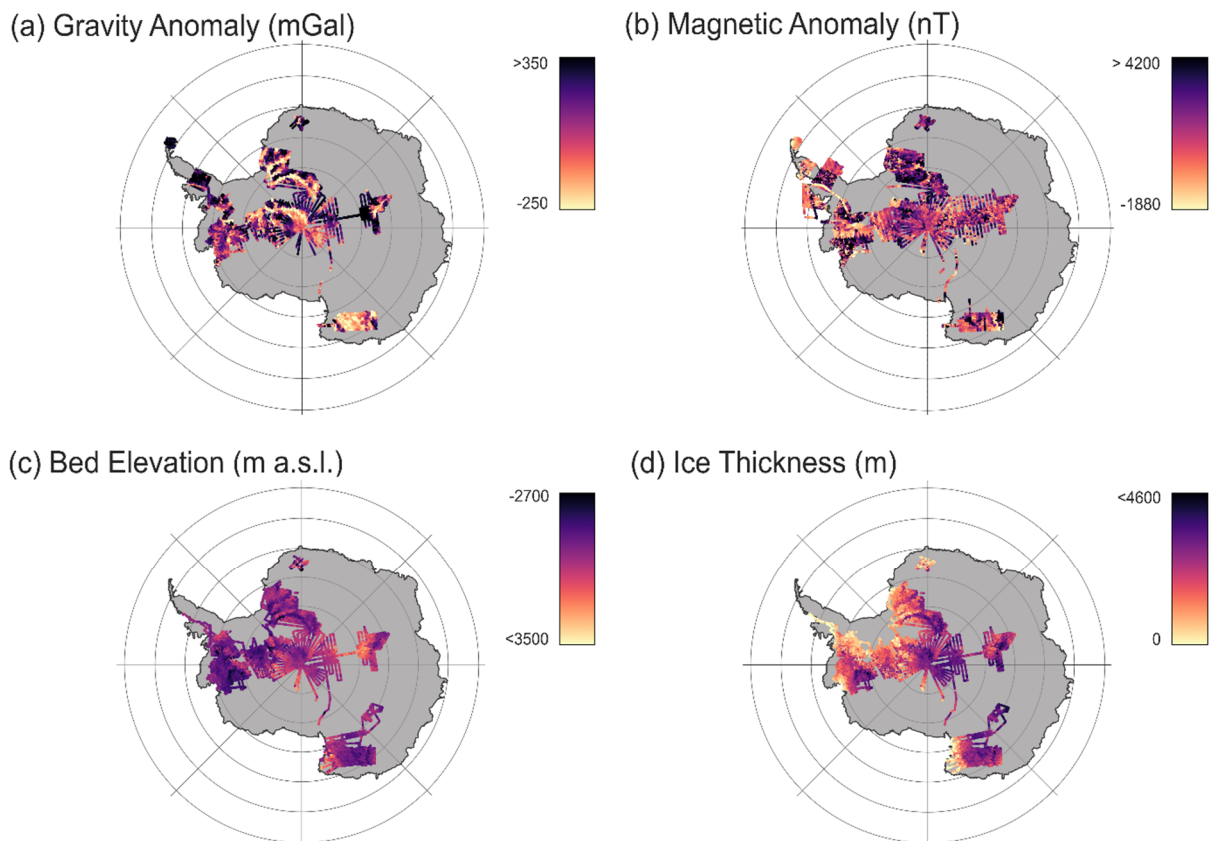
256
257   **Figure 2. Maps of gravity, magnetic, and radar (bed elevation and ice thickness) point**
258   **measurements for all surveys published as part of this data release.** (a) Gravity anomaly points (in milligal,
259   or mGal), (b) Magnetic anomaly points (in nanotesla, or nT), (c) Bed elevation points from radar data (in metres
260   above sea level, or m a.s.l.), (d) Ice thickness points from radar data (metres). In total, this data release consists
261   of 3.62 million gravity, 7.41 million magnetics, and 14.5 million ice-thickness and bed-elevation data points.
262   Note that no correction such as downward continuation has been applied to compile the gravity data shown in
263   (a).

264   The early 2010s saw the deployment of the PASIN system used as part of two large
265   collaborative projects, namely the 2010-11 Institute-Möller Antarctic Funding Initiative (IMAFI)
266   survey over the Institute and Möller ice streams of West Antarctica, and the 2012-13 ICEGRAV
267   survey over the Recovery and Slessor region of East Antarctica.

268   The 2010-11 IMAFI project was a UK initiative between BAS and the Universities of
269   Edinburgh, York, Aberdeen and Exeter. The key aims were to investigate the potential stability of this
270   sector of West Antarctica and test the ability of the subglacial sedimentary structure to control the
271   flow of two large ice streams draining the WAIS into the Weddell Sea Embayment (Ross et al., 2012).
272   Radar data revealed the presence of a reverse-bed slope with a 400-m decline over a 40-km distance
273   away from the grounding line and that this region was relatively close to flotation, indicating the
274   potential instability of this sector in the light of future grounding-line migration upstream of its
275   current position (Ross et al., 2012). Additional analysis using gravity and magnetic data revealed the
276   extent of the Weddell Sea Rift System, adding further evidence for the early-stages of Gondwana
277   break-up and Jurassic extension in the region (Jordan et al., 2013). Further analysis of the radar data
278   acquired during the IMAFI survey led to a new digital elevation model of the subglacial topography
279   around the ice streams of the Weddell Sea Embayment at 1-km resolution, revealing deep subglacial
280   troughs between the ice-sheet interior and the grounding line and well-preserved landforms associated
281   with alpine glaciation (Ross et al., 2014; Jeofry et al., 2018), as well as evidence for a temperate

282 former WAIS via the discovery of extensive subglacial meltwater channels (Rose et al., 2014). The
283 data have also been used to assess the roughness of the subglacial bed (Rippin et al., 2014),
284 investigate englacial properties across the catchment as an indicator of past ice-flow dynamics
285 (Bingham et al., 2015; Winter et al., 2015; Ashmore et al., 2020; Ross et al., 2020), and to evidence
286 the presence of sub-ice shelf channels generated by water flowing from beneath the present ice-sheet
287 (Le Brocq et al., 2013).

288   The 2012-13 ICEGRAV survey, an international collaboration between BAS and the
289 Technical University of Denmark, National Science Foundation, Norwegian Polar Institute, and the
290 Instituto Antártico Argentino, carried out aerogeophysical surveys over the poorly explored Recovery
291 Glacier catchment and Recovery Subglacial Lakes (Forsberg et al., 2018), revealing a deep 800-km
292 trough underlying Recovery Glacier, with evidence for subglacial water controlling the fast flow in
293 the upstream portion of the ice stream (Diez et al., 2018).

294   **2.2.2 2015-2020**

295   The 2015-16 PolarGAP survey was a major international collaboration funded by the
296 European Space Agency (ESA) and led by BAS, Technical University of Denmark, Norwegian Polar
297 Institute and the National Science Foundation to fill a gap in global gravity surveying that the
298 European Space Agency GOCE (Gravity field and steady-state Ocean Circulation Explorer) satellite
299 network was unable to cover. Alongside the large swath of gravity surveying, opportunistic magnetic
300 and radar data were also acquired over the South Pole and parts of Support Force, Foundation, and
301 Recovery ice streams using for a further upgraded radar system, PASIN-2 (see Section 3.1.3).
302 Additional funding from the Norwegian Polar Institute also allowed for a number of dedicated flights
303 over the subglacial Recovery Lakes. The acquired data have led to major scientific findings,
304 including: (a) the presence of anomalously high geothermal heat flux near the South Pole (Jordan et
305 al., 2018), and (b) the delineation of two subglacial lakes (Recovery Lakes A and B) totalling ~4,320
306 km^2 in size and composed of saturated till, with evidence of bed lubrication and enhanced flow
307 downstream of their location as a result of water drainage (Diez et al., 2019). Additional evidence
308 showed that the Pensacola-Pole Basin is characterised by a topographic depression of ~0.5 km below
309 sea level and contains a thick sedimentary layer of 2-3 km in the southern part of the catchment
310 (Paxman et al., 2019). The radar data from the PolarGAP survey have also revealed large troughs at
311 the bottleneck between East and West Antarctica, suggesting that drawdown of the EAIS via the
312 WAIS is unlikely (Winter et al., 2018).

313   In the austral summers of 2015-16 and 2016-17, two surveys were flown as part of the
314 Filchner Ice Shelf System (FISS) project led by BAS and with support from the Alfred-Wenger
315 Institute in Germany and several other UK institutions (UK National Oceanography Centre, Met
316 Office Hadley Centre, and the universities of Exeter, Oxford, and University College London), with
317 the aim to investigate the potential contribution of the Filchner Ice Shelf system to sea-level rise. The
318 2015-16 survey acquired ~7,000 line-km of aerogeophysical data primarily over Foundation Ice
319 Stream and to a smaller extent over Bungenstock Ice Rise. In 2016-17, ~26,000 line-km of
320 aerogeophysical data were acquired over the Academy, Recovery, Slessor, and Support Force
321 glaciers), and parts of the Filchner, and Brunt Ice shelves. Data was also collected over outlet glaciers
322 of English Coast (western Palmer Land, Antarctic Peninsula). Early findings from the 2016-17
323 aerogeophysical survey revealed subglacial drainage channels beneath Support Force Glacier
324 (Hofstede et al., 2021), provided evidence for a large ~80 x 30 x 6 km mafic intrusion likely resulting
325 from mantle melting during Gondwana break-up (Jordan and Becker, 2018), and helped to delineate
326 the subglacial bathymetry beneath Brunt Ice Shelf (Hodgson et al., 2019).

327   During the 2018-19 and 2019-20 seasons, BAS was involved in aerogeophysical surveying of
328 Thwaites Glacier as part of the UK-US International Thwaites Glacier Collaboration (ITGC)
329 initiative. The 2018-19 survey acquired ~9,900 km of aerogeophysical data over lower Thwaites

Glacier and Thwaites Glacier Ice Shelf, and the 2019-20 survey acquired ~4,500 line-km over lower Thwaites Glacier, the WAIS Divide ice-core site, and Rutford Ice Stream. These surveys contributed to a new bathymetric map of Thwaites, Crosson and Dotson ice shelves from gravity measurements, revealing a deep (>800 m) marine channel extending beneath the ice shelf adjacent to the front of Thwaites Glacier (Jordan et al., 2020). These datasets have also contributed to a new bathymetry model of George VI Sound (Constantino et al., 2020) and were integrated with swath bathymetric data out-board from Thwaites Glacier (Hogan et al., 2020).
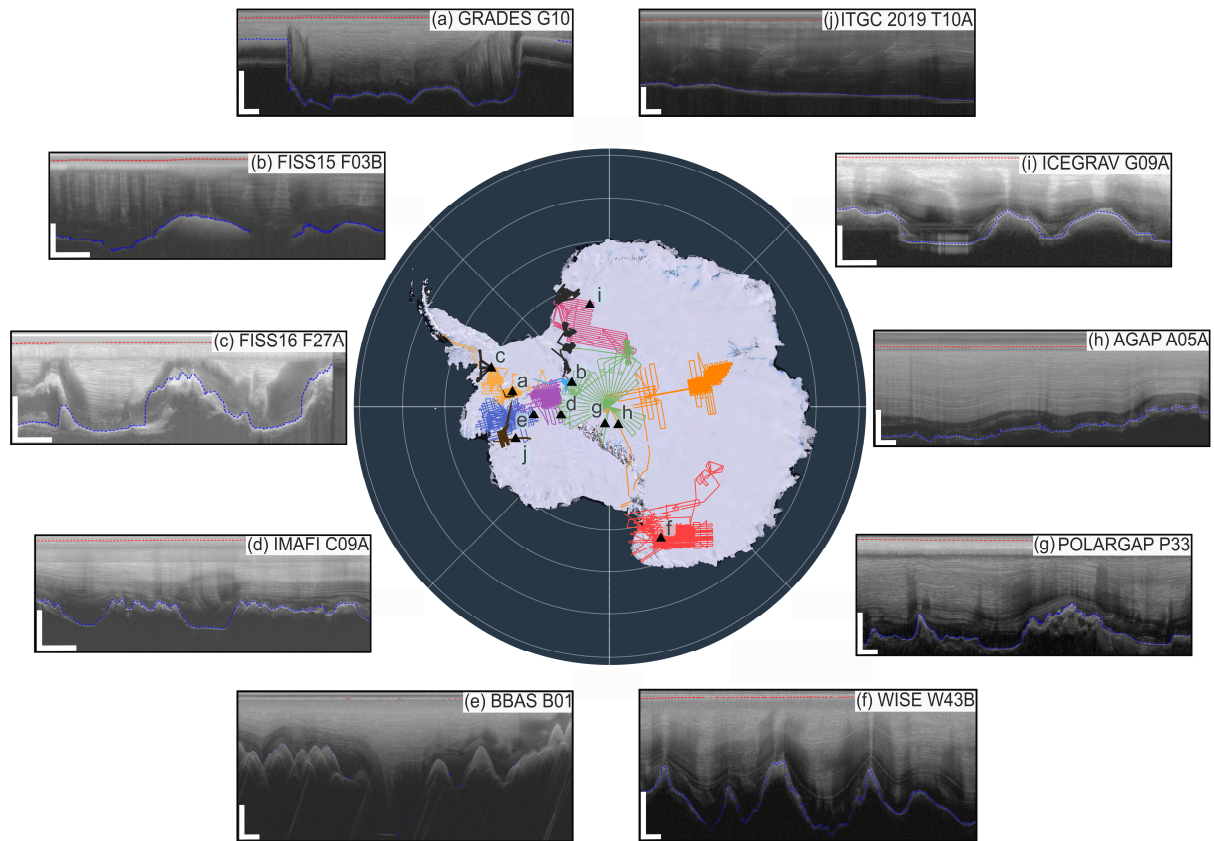
Figure 3. Sample radargrams from the ten 2-D radar datasets released with this paper. The colours for each survey on the map are the same as in Fig. 1 and the data portal. The location of each radargram (a-j) is marked on the map by black triangles. The red and blue dashed lines on the radargrams are the surface and bed picks, respectively. A description of each radargram is provided as follows: (a) Flightline G10 (GRADES-IMAGE) showing well-defined subglacial valleys through which Evans Ice Stream flows (ice flow is approximately out of page), with stable layering at the onset and in the middle of the topographic low; (b) Flightline F03B (FISS 2015) showing undulating bed topography and disrupted layering at the onset of Foundation Ice Stream; (c) Flightline F27A (FISS 2016) showing variations in subglacial topography at the divide between the Antarctic Peninsula and West Antarctica, with potential evidence of basal freeze-on at the start of the segment; (d) Flightline C09A (IMAFI) showing evidence of preserved layering despite changes in local topography at the bottleneck between East and West Antarctica; (e) Flightline B01 (BBAS) over Ellsworth Subglacial Mountains showing a ~1.5 km trough in the ice sheet bed and one of the deepest points in the PIG basin with ~3km of ice underlying the surface; (f) Flightline W43B (WISE-ISODYN) showing internal layers draping over the highs and lows in the local Wilkes Subglacial Basin topography, with two particularly bright reflections in the middle and bottom of the ice column; (g) Flightline P33 (PolarGAP) showing the onset of a topographic high near the Transantarctic Mountain Range with internal layering visible down to the ice-bed interface; (h) Flightline A05A (AGAP) showing stable internal layering characteristic of the interior of the EAIS; (i) Flightline G09A (ICEGRAV) showing evidence of a bright reflection likely associated with a previously unidentified subglacial lake in the region; and (j) Flightline T10A (ITGC 2019) showing a section of inland-sloping bed from a profile in the main trunk of Thwaites Glacier, >200 km from the current grounding line position (ice flow is right to left). The horizontal and vertical white bars at the bottom of each radargram

359 represent ~3 km in the horizontal direction (i.e. distance) and ~1 km in the vertical direction (i.e. depth)
360 respectively.

361

3. Data Acquisition and Processing

363    The typical acquisition and processing workflow for the aerogeophysical data is shown in
364 Figure 4. Usually, the aircraft is set up systematically to acquire gravity, magnetic, and radar data
365 together, except in situations where surveying objectives are not compatible with the acquisition of all
366 three datasets at once (i.e. flying at constant terrain clearance for the radar data affects the quality of
367 the gravity data which is better flown at constant altitude, and vice-versa); although novel gravity-
368 acquisition methods are increasingly making this issue redundant (see Section 3.1.1). As shown in
369 Table 1, the conventional gravity-magnetic-radar set-up was used in 15 out of 24 surveys, with the
370 remaining seven campaigns using either a magnetic-radar- or gravity-magnetic-only set-up and only
371 two using a magnetic-only set-up. The data acquisition steps for each type of data are described in
372 Section 3.1, and the processing of the data is described in Section 3.2.
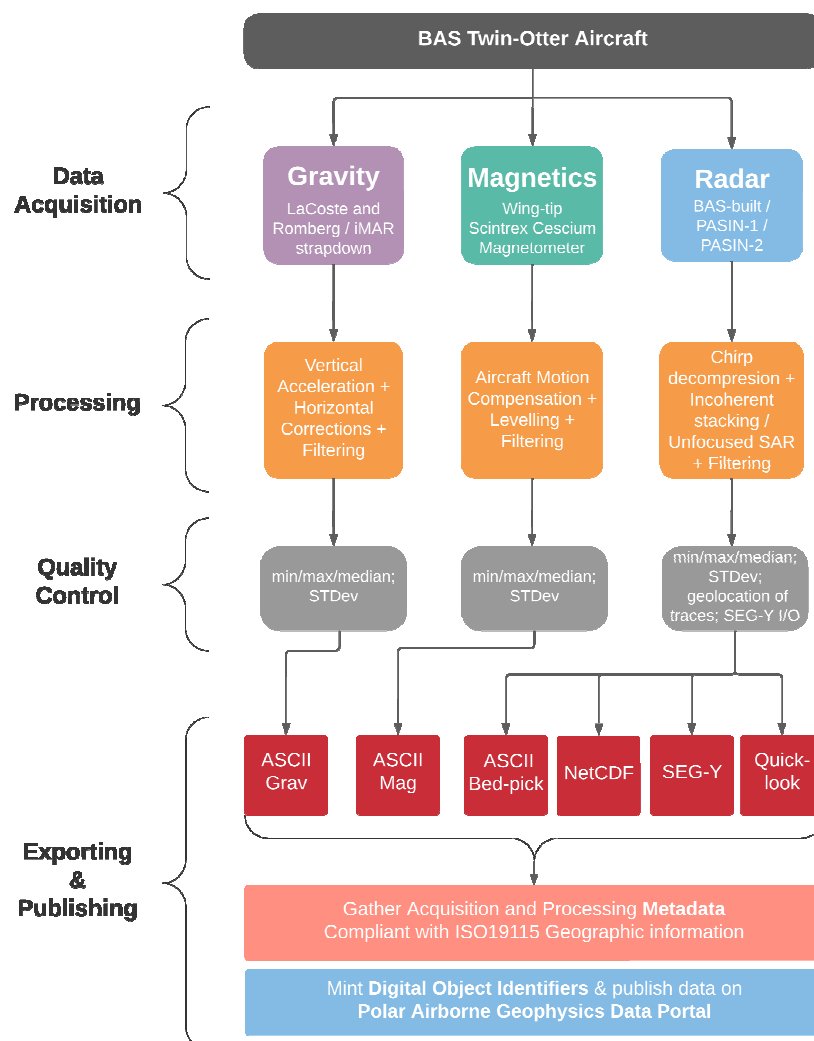
373

374 **Figure 4. Workflow describing the data acquisition, processing, and publishing for the BAS**
375 **aerogeophysical data included in this data release.** "STDev" stands for standard deviation, whilst "I/O" refers
376 to the output of the SEG-Y files and the import of the files into seismic-interpretation software for quality check.

3.1. Data Acquisition and Instrumentation

378 All BAS aerogeophysical data acquisition is conducted using Twin Otter aircraft due to their
379 remote capabilities, long fuel range (up to 1,000 km), and operability. The aircraft's twin turbo-prop
380 engines enable it to conduct rapid take-off and landing and operate in small and remote airfields
381 commonly covered in snow and icy terrains using mounted skis. All data acquisition since the early
382 1990s has been conducted using the BAS DeHavilland Twin Otter aircraft "VP-FBL" (Fig. 5). The
383 aircraft typically flies at a nominal speed of ~60 m/s, which results in an along-track distance between
384 each stacked radar trace of 0.2 m (prior to processing). The following sections describe the acquisition
385 of the data for the gravity (3.1.1), magnetic (3.1.2), radar (3.1.3), and GPS and lidar (3.1.4)
386 instruments on board the aircraft.
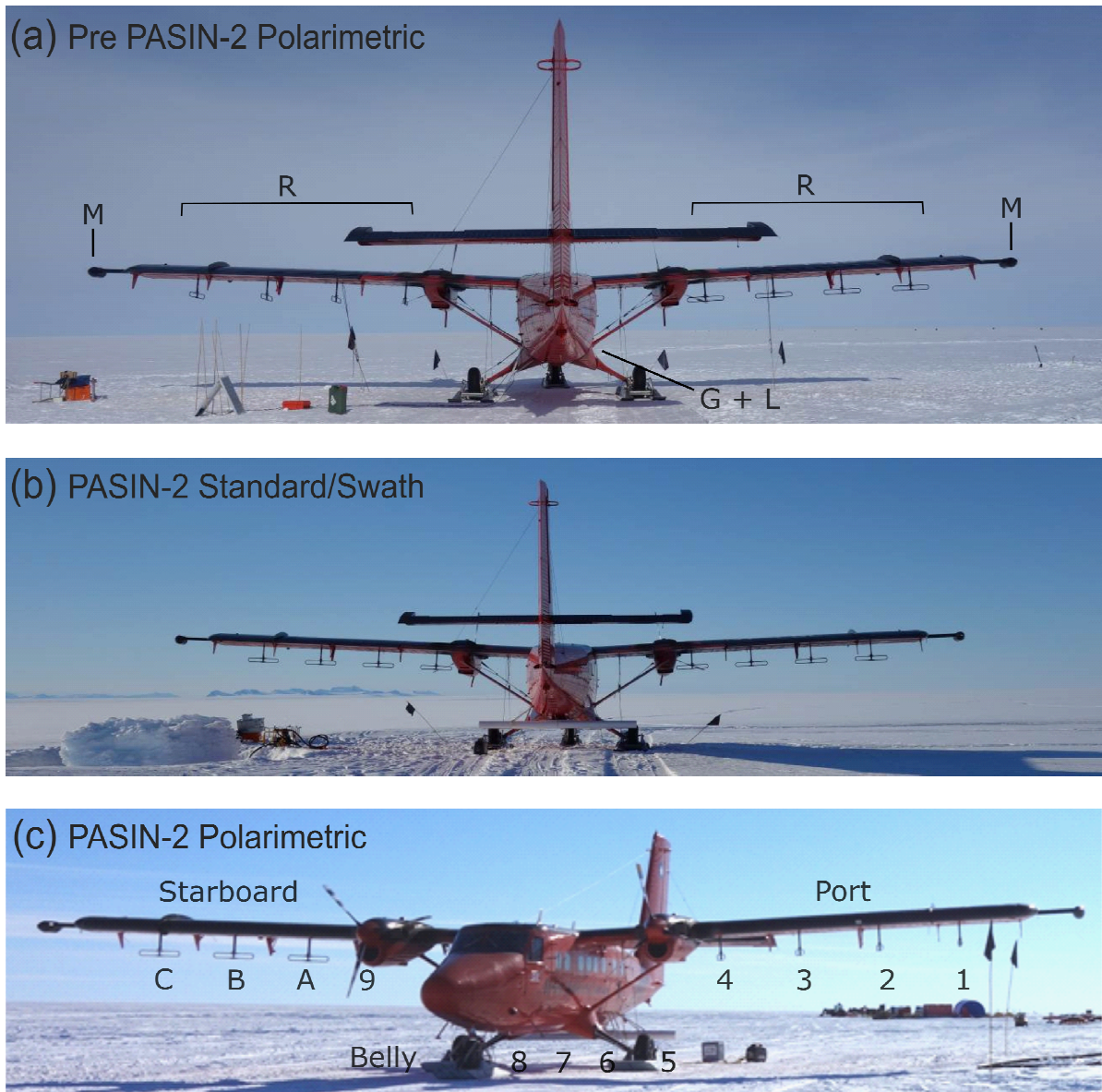
387

388 **Figure 5. Photographs of the aerogeophysical set-up on the BAS Twin Otter aircraft "VP-FBL"**
389 **for PASIN-2.** (a) The pre-PASIN-2 (used in 2015-16 PolarGAP only) configured to mimic the set-up of
390 PASIN-1 data collection in polarimetric mode. The eight folded dipole transmitting and receiving antennas are
391 fixed under the wings (two transmit and two receive antennas on each wing) with the port configured as V
392 (vertical) and starboard as H (horizontal). The annotations show the location of the radar (R), magnetic (M), and
393 gravity and lidar (G + L) instruments on board the aircraft. (b) The PASIN-2 set-up in standard/swath mode.
394 The eight folded dipole transmitting and receiving antennas are fixed under the wings and inside the aircraft and
395 are operated using a RF (Radio Frequency) switch, and an additional four receiving antennas are situated in the

belly enclosure. When in standard swath mode, all antennas are configured in H orientation with the starboard and belly antennas also in H orientation. The PASIN-1 set-up in standard mode (not shown here) had a similar configuration as shown in (b) bar the belly antenna (i.e. only four transmit on port and four receive on starboard in H orientation) (c) The PASIN-2 set-up in polarimetric mode. The eight folded dipole transmitting and receiving antennas are fixed under the wings and inside the aircraft and are operated using an RF switch, and an additional four receiving antennas are situated in the belly enclosure. When in polarimetric mode, the port antennas are configured in V orientation and the starboard and belly antennas in H orientation. The PASIN-1 set-up in polarimetric mode (not shown here as rarely flown) had the two pairs of outboard antennas rotated to V and the inboard in H configuration. Photo credit: Carl Robinson.

3.1.1 Gravity

Until 2012, BAS aerogravity measurements were acquired with a LaCoste and Romberg air-sea gravimeter modified by Zero Length Spring Corporation (ZLS). The gravimeter was mounted in a gyro-stabilised, shock-mounted platform at the centre of the aircraft to minimise the effect of vibrations and rotational motions.

Starting with the 2015-16 PolarGAP survey, aerogravity data began to be aquired using a novel strapdown method which, unlike traditional surveys using a stabilised gravity platform, allowed for the collection of gravity data during draped or turbulent flights (Jordan and Becker, 2018). For this survey, both the LaCoste and Romberg and the strapdown systems were operated together with results from the two systems merged to provide an optimum data product with the long-term low and predictable drift of the LaCoste and Romberg system and dynamic stability of the strapdown system. Subsequent surveys used a strapdown sensor alone, removing the need to prioritise the quality of the gravity data over the radar data and allowing for flights at a constant terrain clearance for optimal radar-data collection. The optimum resolution of the system is approximately 100 s along-track (Jordan and Becker, 2018).

The first strapdown sensor deployed by BAS was the iMAR RQH-1003 provided by Technical University (TU) Darmstadt, and consisting of three Honeywell QA2000 accelerometers (mounted in mutually perpendicular directions) and three Honeywell GG1230 ring laser gyroscopes. The subsequent 2018-19 and 2019-20 ITGC surveys over Thwaites Glacier used the iMAR iCORUS strapdown airborne gravimeter systems from Lamont-Doherty Earth Observatory and BAS respectively, which have approximately equivalent internal components to the TU Darmstadt system.

3.1.2 Magnetics

The Twin Otter is configured for fixed wing magnetometer operation. The aircraft modifications include inboard-positioned wingtip fuel pumps, pod-boom hard points and a demagnetised airframe to maximise magnetic-data collection. Scintrex CS3 Cesium sensors are used due to their high sensitivity, high cycling rates, excellent gradient tolerance, fast response and low susceptibility to the electromagnetic interference. The resolution of the magnetometers has greatly increased over time, with the current systems having a measurement accuracy of 0.2 pT compared with the older systems used between 1991-2003 (10 pT; Sintrex H8 Cesium) and 1973-1990 (500 pT; Geometrics G-803 Potassium).

3.1.3 Radar

Prior to 2004, BAS deployed a custom-built, 8-array element radar system, referred here as "BAS-built" (Corr and Popple, 1994). This was a coherent radar system operating at a centre frequency of 150 MHz and using a transmit power of 1,200 W (Rippin et al., 2003a). The radar system was equipped with eight folded dipole transmitting and receiving antennas fixed under the wings (four transmitting on port wing, four receiving on starboard wing). Similar to the current systems, the "BAS-built" system transmitted both a conventional narrow-sounding pulse mode of 0.25 μs and a deep-sounding 4μs, 10-MHz chirp (Table 2). As developments in digital acquisition

became commercially available, several technical upgrades were applied to the radar system. These ranged from using a LeCroy scope to acquire logarithmic detected waveforms to accomodate complex coherent acquisition, as well as the replacement of the LeCroy oscilloscope by a low sample-frequency 12-bit dual ADC (analogue-to-digital converted) card in the later years of operation (see Figure S1). During this time, the dynamic range of the system was extended by the interleaved transmission of different waveform, which were conventional short wavetrain pulses at the centre frequency.

After operating for ten successive field seasons, the "BAS-built" radar system was retired and replaced by a more modern radar system, the Polarimetric Airborne Survey INstrument (PASIN) (Corr et al., 2007). In contrast to the "BAS-built" system, PASIN was designed to sound ice much deeper (up to 5 km compared with 3.3 km for the earlier system) thanks to improved digital electronics and added power in the transmitting antennas (see Table 2). Additionally, modern methods of digitisation enabled by the use of ADC cards, rather than a digitising scope, allowed phase and not just power to be recorded in greater resolution on PASIN, which eventually allowed for the use of more advanced processing techniques such as Synthetic-Aperture-Radar to be applied to the data (see Section 3.2.3).

The older PASIN-1 (2004-2015) and the newer PASIN-2 (2015-Present) systems are bi-static radars operating at a 150-MHz centre frequency and configured as follows: (a) PASIN-1: 10-MHz bandwidth system with eight folded dipole transmitting and receiving antennas fixed under the wings (four transmitting on port wing, four receiving on starboard wing) operating in H (horizontal) orientation when in standard mode and more rarely with the port (transmit) and starboard (receive) antennas positioned in both H and V (vertical) orientation when in polarimetric mode (see similar PASIN-2 set-up in Figure 5a) (Corr et al., 2007); and (b) PASIN-2: 13-MHz bandwidth system with eight folded dipole transmitting and receiving antennas fixed under the wings and inside the aircraft with RF switches and an additional four receiving antennas in the belly enclosure (see Figure 5b-c; Table 2). The main difference between the PASIN-1 and -2 systems is the ability for across-track swath processing to be applied to the PASIN-2 data by allowing both transmit and receive on the folded dipole antenna via the use of RF switches.

In further contrast with PASIN-1, the PASIN-2 radar has a very flexible configuration, with the standard configuration being as a twelve channel swath radar (with eight transmit and twelve receive). However, other configurations are also possible, including a polarimetric mode to give H and V data where the port antennas are rotated 180 degrees (see Table S1). A final configuration is a mixed antenna gain path for areas where ice is heavily disrupted and where the starboard signal can be attenuated by several decibels. Since 2016, the PASIN-2 system has undergone minor modifications to reduce noise and improve system operations, including (a) low-pass filters in the RF switches, (b) the use of a 10-GHz waveform generator, and (c) new 1 kW solid-state power amplifiers which have lowered transmit system noise and increased transmitter and receiver isolation.

Data for both versions of the PASIN system are received using sub-Nyquist digitisation and stacking and stored on removable solid-state disks or tapes, and then copied to duplicate spinning disks for data archiving. On average, a 4.5-hour flight will generate ~150-200 GB of data for PASIN-1 and up to 3 TB of data for PASIN-2. The systems systematically acquire a shallow-sounding 0.1 μs pulse (PASIN-1) / 1 μs short-attenuated chirp (PASIN-2), and a deep-sounding 4 μs, 10-MHz (PASIN-1) /13-MHz (PASIN-2) linear chirp (Table 2). The shallow-sounding pulse/short-attenuated chirp product is best used to assess internal layering in the upper ~1.5-2 km of the ice sheet, whereas the deeper-sounding chirp is best suited to assess englacial layering and bed characteristics in deep-ice conditions (Fig. 6 c-e). The radar is capable of sounding ice to depths of up to 5 km with a horizontal resolution of 10 cm (before processing) and a depth resolution in the vertical direction of 8.4 m (PASIN-1) and 6.5 m (PASIN-2).

Table 2. Radar Parameters for the three radar systems deployed by BAS between 1994 and the Present. Note that PASIN-1/2 have a number of programmable settings for flight-specific objectives (e.g. 1 to 8 waveforms programmable for PASIN-2), and the numbers provided here are for the most commonly used settings. For PASIN-2, a standard set-up consists of 5 waveforms as follows: 4 μs H (0°), 4 μs V (0°), 4 μs H (90°), 4 μs V (90°) ,1 μs H (Table S1). Abbreviations in the table are as follows: ADC = Analogue to Digital Converter; FPGA = Field Programmable Gate Array; SF = Sample Frequency; SI = Sample Interval; PRF = Pulse-Repetition Frequency; PRI = Pulse Repetition Interval. *BAS-built and PASIN-1 systems used RF combiners on the receiver to produce a single RF input-to-sample, with PASIN-1 splitting these into a high and low gain channel for standard mode (2 ADC channels) and combining these for pairs of H and V in polarimetric mode (4 ADC channels). **Radar Range Resolution is calculated using a radiowave velocity in ice of 168 m/microseconds and does not include the effect of the processing on the vertical resolution of the system which is expected to be ~50% greater than the values provided in the table, thus these numbers should be interpreted as the theoretical system performance. Diagrams showing the configurations of the three radar systems are provided in the Supplementary Information (Fig. S1-3).

Radar Parameters	BAS-built (1994-2004)	PASIN-1 (2004-15)	PASIN-2 (2015-Present)
Antennas Configuration	8x folded dipole (4 Tx / 4 Rx)*	8x folded dipole (4 Tx / 4 Rx)*	8x folded dipole + 4x belly (8 Tx/Rx + 4 Rx only)
Centre Frequency	150 MHz	150 MHz	150 MHz
Transmitted Pulse Width	0.25 μs (pulse) 4 μs linear (chirp)	0.1 μs (pulse) 4 μs linear (chirp)	1 μs (Tukey envelope chirp) 4 μs linear (Tukey envelope chirp)
Chirp Bandwidth	4 MHz (pulse) 10 MHz (chirp)	10 MHz	13 MHz
Antenna Gain	11 dBi	11 dBi	11 dBi
PRF / PRI	20,000 Hz (PRI: 50 μs)	15,635 Hz (PRI: 64 μs)	15,635 Hz (PRI: 64 μs)
Peak Transmit Power	300 W / antenna (1.2 kW total)	1 kW / antenna (4 kW total)	1 kW / antenna (8 kW total)
Receiver SF	25 MHz (scope max single shot)	88 MHz	120 MHz
Receiver FPGA decimation	-	4	-
Receiver Effective SF	25 MHz (SI: 40.0 ns)	22 MHz (SI: 45.5 ns)	120 MHz (SI: 8.3 ns)
Receiver Trace Stacking	64	25 (standard) 50 (polarimetric)	25
Effective PRF (post-stacking)	312.5 Hz	312.5 Hz (standard 2 waveforms)	125.1 Hz (5 waveforms) 208.5 Hz (3 waveforms)
ADC Resolution	12-bit	14-bit	16-bit
Equivalent Sustained Data Rate per ADCs (FPGA)	100 MB/s	176 MB/s (standard) 352 MB/s (polarimetric)	960 MB/s (system: 2.88 GB/s)
Average Data Storage Rate for Full PRI	~1 MB/s	11 MB/s (maximum)	173 MB/s (all arrays)
Radar Range Resolution**	21.0 m (pulse) 8.4 m (chirp)	8.4 m	6.5 m

The pulse repetition frequency of the PASIN (1/2) system is 15,635 Hz and hardware stacking is typically set to 25 in standard mode, which results in an effective pulse-coded waveform acquisition

508 rate of 312.5 Hz for each transmit pulse (Table 2). Following stacking, the final sampling frequency
509 of PASIN-1 is 22 MHz and PASIN-2 is 120 MHz (Table 2).

3.1.4 GPS and lidar

511   Since 1978, navigation has transitioned from basic aircraft data, imagery, and dead reckoning
512 to more modern means, including the use of carrier-phase Global Positioning System (GPS) systems.

513   Between 1994 and 2004, the BAS Twin Otter aircraft was equipped with a Trimble GPS
514 system (1994-95 surveys: Trimble 4000SSE; 1996-2003 surveys: Trimble 4000SSI). Since 2004, the
515 aircraft is equipped with two, 10-Hz GPS receivers (Leica 500 and ASHTEC Z12 for 2004-18
516 surveys; Javad Delta and Novatel Span for post-2018 surveys) installed on board the aircraft. On the
517 ground, two Leica 500 GPS base stations (replaced by Javad TRIUMPH-2 for post-2018 surveys) are
518 positioned and equipped with choke-ring antennas set up specifically to obtain an unobstructed view
519 of the sky above. Aircraft turns are typically limited to 10-degree banking angles in order to avoid
520 losing lock with GNSS satellites orbiting close to the horizon. The estimated accuracy of the absolute
521 position of the aircraft is 10 cm or less, with the relative accuracy approximately one order of
522 magnitude better. Since 2010, the aircraft altitude and inertial information has been provided by an
523 iMAR FSAS inertial measurement unit (IMU), with the data logged on a Novatel Span receiver.
524 Additional attitude information from the strapdown gravity system is also available for post
525 processing of other datasets.

526   For all modern surveys, the aircraft was also equipped with a Riegl Q240i-80 laser altimeter
527 system (or lidar) in the floor camera hatch to accurately detect the ice surface. The lidar data used for
528 correction of the radar data are typically extracted from the nadir point value with no correction for
529 aircraft altitude. The system has a repetition frequency up to 2 kHz which results in an along-track
530 measurement every 3 cm with an accuracy of up to 5 cm. The lidar is used up to altitudes of 700 m
531 and is constrained by cloud/fog-free conditions. From 2010 onwards, the lidar onboard the Twin Otter
532 was capable of obtaining swath lidar data, although only the single-point data along the centre line is
533 provided as part of this data release.

3.2. Data Processing

3.2.1 Gravity

536   The raw aerogravity data are processed to obtain levelled free-air gravity anomalies.
537 Although additional survey-specific processing might have been applied to the data, general
538 processing steps for the LaCoste and Romberg system include the calculation of the observed gravity
539 and a range of corrections and filtering functions as described in Jordan et al. (2007; 2010) and
540 Valliant (1992). In particular, corrections for vertical acceleration, Eotvos horizontal motion (Harlan,
541 1968), latitude (Moritz, 1980), and free air (Hackney and Featherstone, 2003) were applied to obtain
542 the final free-air anomalies before subsequent 9-12 km low-pass filtering. As the free-air values refer
543 to the WGS84 ellipsoid, they are defined in geodesy as gravity disturbance (Hackney and
544 Featherstone, 2003).

545   The strapdown gravity method adopted from 2015-onwards directly combined observations
546 of acceleration in all three axes, with orientation and GPS observations combined in a Kalman filter to
547 solve simultaneously for aircraft position and variations in Earth's gravitational field (Becker et al.,
548 2015). For subsequent strapdown-acquisition surveys, some amount of levelling/correction for
549 thermal drift are required. Spectral analysis suggests that the strapdown system can resolve
550 wavelengths on the order of ~5 km (Jordan et al., 2020). Error estimates for the gravity data can be
551 found in the respective survey metadata (see Table 3), or in specific studies utilising the BAS
552 aerogravity data (e.g. Ferraccioli et al., 2006; Forsberg et al., 2018; Jordan and Becker, 2018).

Additional processing may include the use of masks to remove aircraft turns, start and end of lines, and other regions of noisy data, or producing an upward continued free-air anomaly by upward continuing each line segment from the collected flight altitude to the highest altitude in the survey. The first level of free-air anomaly for all published BAS data is shown in Figure 2a, although it is worth noting that no correction such as downward continuation has been applied to compile the data shown in Figure 2a. It is considered that at the scale of the map, the vertical gradient of residual gravity anomalies at flight altitude is inferior to 2 mGal. Additionally, as the gravity surveys are acquired over the ice sheet, the distance to the bedrock is not only dependent on the flight altitude but also on the ice thickness.

3.2.2. Magnetics

The raw aeromagnetic data have been processed using the SCAR ADMAP2 data-release protocols (Golynsky et al., 2018). Data were collected at 10 Hz, allowing for modelling and removal of aircraft dynamic movements using a so-called compensation correction (Ferraccioli, et al. 2007). This correction typically requires a dedicated calibration flight in the direction of the survey lines and tie-lines to have been flown. For some surveys with radial design, or where magnetic-data acquisition was opportunistic, logistical constraints meant no calibration flight could be conducted. In these cases, the generally large depth-to-source due to the thick ice allowed for a 10- to 15-second filter to be applied to minimise noise generated by aircraft motion without compromising the geological signal. Given the redundancy of collecting 10 Hz (~6 m spaced) observations over thick ice, most surveys were down-sampled to 1 Hz (~60 m) prior to further processing.

After magnetic compensation, the magnetic data were corrected for the International Geomagnetic Reference Field (IGRF), which is a standard mathematical description of the Earth's main magnetic field. Data impacted by operation of aircraft systems such as pumps and heaters were manually determined. Typically such data were discarded, but survey design and lack of alternative data sources mean that sometimes important geophysical signatures may be present. In some cases the contaminated data were therefore corrected using an offset correction, accepting that the data segment may be more noisy.

Magnetic data were then corrected for diurnal variations in the magnetic field using observations at a fixed base station, typically filtered with a 30-minute filter to remove short-wavelength noise potentially not seen on the aircraft. Further statistical levelling of the data based on internal intersections and crossovers with previous surveys was carried out at times to remove systematic errors associated with flight direction (i.e. heading corrections) and additional long-wavelength errors associated with incomplete removal of diurnal variations. In some cases, continuation to a fixed altitude above the ice-sheet bed and a final grid-based micro-levelling procedure was applied (Ferraccioli et al. 1998). The magnetic anomaly map shown in Figure 2b shows the spatial coverage and magnitude of magnetic data available. Errors in the data are typically presented as the standard deviation of the crossover errors and can be found in the respective survey metadata (see Table 3).

3.2.3. Radar

All data acquired with the earlier "BAS-built" radar system (1994-2004) were read using a C code software to convert the LeCroy data to formats readable by Halliburton Landmark's seismic-processing software SeisSpace ProMAX, hereafter referred to as ProMAX. Basic processing was applied to the data in the hardware analogue domain and later using ProMax, including power normalisation and final SEG-Y export. Following the transition from the LeCroy oscilloscope to ADC cards on the "BAS-built" system (see Section 3.1.3), MATLAB replaced the IDL language for data processing.

599   As opposed to the "BAS-built" system which, by design, had some level of processing done
600   on the raw data internally, the PASIN system was designed to retain much of the sampled data in the
601   rawest form possible to allow for evolving processing techniques to be applied to the data in the
602   future. For all PASIN data (2004-onwards), the first high-level step was to extract the raw data from
603   the tape drives, convert the three-byte values to conventional four-byte integers, combine the
604   waveforms associated with each pulse transmit type, and then export the data into MATLAB-
605   formatted binary files. The second high-level step was to minimise sidelobe levels by applying a
606   chirp-decompression technique using a Blackman window from a custom-built MATLAB toolbox,
607   resulting in a processing gain of ~10 decibels (dB).

608   The next step was to apply processing techniques both to enhance along-track resolution and
609   improve the signal-to-noise ratio. For the 2004-05 BBAS survey, incoherent stacking of 10
610   consecutive traces was applied and a moving-average window filter used; however, no Synthetic
611   Aperture Radar (SAR) techniques were initially applied to these data. First tested on previously
612   acquired PASIN radar data (see Hélière et al., 2007), 2-D SAR processing based on the Omega-K
613   algorithm and subsequently improved versions using Doppler-beam sharpening were applied
614   systematically to all the deep-sounding chirp data from 2005-2006 onwards to increase spatial
615   resolution and remove backscattering hyperbolae in the along-track direction (Corr et al., 2007; Jeofry
616   et al., 2018). The benefit of using unfocused along-track SAR processing is that it resolves the bed in
617   much finer detail compared with non-SAR focused data (see Figure 6 d-e); however, SAR-processing
618   can also lead to distortions of the amplitude of the ice structure and bed reflection in unhomogenous
619   areas of the ice sheet (e.g. near grounding line; see Hélière et al., 2007) and thus might not always be
620   appropriate for assessing internal layering or absolute amplitudes such as required for bed-reflectivity
621   analysis (e.g. Peters et al., 2007; Castelletti et al., 2019). Additional moving-average filters of varying
622   lengths have also been applied to enhance englacial reflections and improve visualisation of the radar
623   data.

624   Figure 6 shows the three processed radar products provided for the 2010-11 IMAFI survey
625   over West Antarctica. Figure 6c shows the shallow-sounding pulse and Figures 6d-e the deep-
626   sounding chirp radar data using the unfocused SAR-processing technique from Hélière et al. (2007)
627   (Fig. 6d) and a version of the chirp product processed with coherent summations but with no SAR-
628   processing applied (Fig. 6e). Internal layering is more clearly visible in the upper part of the ice
629   column on the pulse data compared with the chirp data (see black-bordered insets in Fig. 6c and 6e).
630   In contrast, deeper internal layering is much more visible on the SAR-chirp than the non-SAR chirp
631   (Fig. 6d-e). Additionally, the peak amplitude of the bed is better resolved in the SAR-processed chirp
632   than the non SAR-processed chirp (see white-bordered inset in Fig. 6d-e).

633
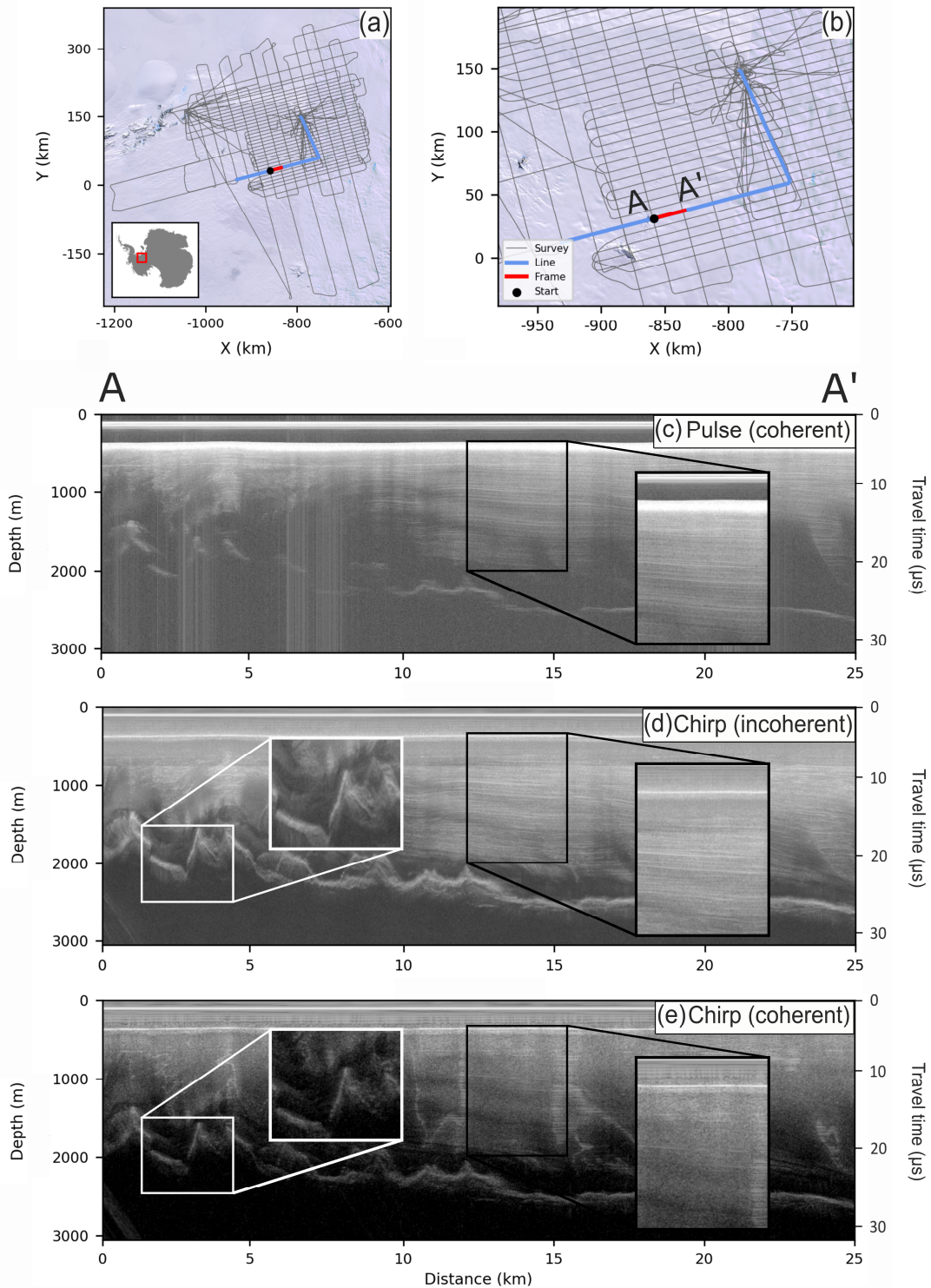
Figure 6. A 25-km segment for flightline 15d of the 2010-11 IMAFI survey showing the three radar products and processing attributes. (a) shows an overview map of the entire survey with an inset over Antarctica and (b) shows a zoomed-in map over the specific flightline with the 25-km radar segment (defined as A-A') shown in red. The background satellite image in (a-b) is from the Landsat Image Mosaic of Antarctica (LIMA) (Bindschadler et al., 2008). (c-e) show a 25-km segment of the data for the three products provided for the 2010-11 IMAFI survey as follows: (c) the coherently processed, shallow-sounding pulse, (d) the unfocused 2-D SAR-processed, deep-sounding chirp, and (e) the coherently processed, deep-sounding chirp. The black-bordered insets zoom to the internal layering in the upper portion of the ice column for (c-e) and the white-bordered insets show the difference in bed characteristics between (d-e).

643   Further processing of the PASIN data has also been applied by others using simple image-
644 processing techniques such as moving-average filters to enhance the internal layering of the ice and
645 reduce incoherent noise (Ashmore et al., 2020; Bodart et al., 2021), or by applying more complex
646 SAR processing techniques over previously incoherently processed radar data (Castelletti et al., 2019;
647 Chu et al., 2021). Additional techniques have also be employed in areas where side-echos from steep
648 valley walls lead to ambiguous bed reflections, as previously employed over Flask Glacier (Antarctic
649 Peninsula) using PASIN SAR-processed data and a combination of velocity and digital elevation
650 models to obtain more accurate ice thickness estimates (Farinotti et al., 2013).

651   Following radar data processing, bed and ice-surface reflections were determined by picking
652 the onset of the basal echo (i.e. where the echo amplitude is greater than the noise floor). We note that
653 this is not a universal method applied by all radar data providers, who, may pick the half-amplitude
654 delay or the peak value, leading in turn to measurement biases across data providers and products (e.g.
655 Peters et al., 2005; Chu et al., 2021).

656   The BAS approach to picking the bed was to use a semi-automatic first-break pick algorithm
657 on the chirp data below a top-mute window in ProMax (generally ~100 samples above the
658 approximate bed reflection) to locate the precise bed return, followed by manual checks and re-
659 picking to exclude any unrealistic spikes. In areas where multiple closely spaced reflections were
660 sounded at the bed, the shallowest reflection was assumed to be the bed as off-axis reflections would
661 likely appear lower down in this section. However, in some cases, reflections, which appeared deeper,
662 were chosen, with shallower weak reflections assumed to reflect entrained debris, accreted ice, or
663 uncompensated refraction hyperbolae close to the bed. We note, however, that this method has
664 evolved over the years, and that its success is inherently reliant on the radioglaciological experience
665 of the human picker to quality-check the results from the semi-automatic picker and manually re-pick
666 the data if necessary. The uncertainty associated with the picking procedure can be partially
667 approximated by calculating the Root-Mean-Square error (RMS) of the bed elevations at crossover
668 points across the survey area. Although these errors are site-specific and can depend on factors such
669 as varying bed topography and roughness, larger errors may reflect uncertainties in data processing or
670 analysis (i.e. picking in this case). Areas of more extreme topography typically show the highest
671 crossover errors, likely associated with off-axis reflections and entrained debris close to subglacial
672 cliffs, which make deciding on the correct bed pick challenging. In isolated cases, such errors can
673 exceed several hundred meters. In contrast, regions dominated by smooth and flat bed typically show
674 lower crossover errors, on the order of several meters only. Survey wide RMS errors are typically
675 reported in each survey's metadata (see Table 3) and average ~9 to 22 m depending on the survey (see
676 Rippin et al., 2003; Vaughan et al., 2006; Ross et al., 2012; Jeoffry et al., 2018).

677   To estimate ice thickness and hence obtain the bed elevation, the location of the surface
678 reflection in the radar data must be known accurately. However, since the PASIN system does not
679 resolve the ice surface well due to errors in the phase centre of the pulse through the firn layer, the
680 surface reflection in the radargram was only rarely used on its own to calculate the ice surface.
681 Usually, range-to-surface from coincident on board-acquired lidar, or alternatively if lidar was not
682 available (i.e., due to clouds or ground clearance higher than 750 m), using the aircraft's radar
683 altimeter or surface elevation from an accurate Digital Elevation Model (DEM) (i.e. REMA 8-m
684 DEM for latest surveys; Howat et al., 2019), was used to calculate a "theoretical" surface pick, as
685 follows:

686   Firstly, the same semi-automatic picker used for picking the bed was used on a subset of the
687 shallow-sounding pulse radargrams with a bottom-mute window set at ~100 samples below the
688 surface reflection. Secondly, once aircraft-to-surface range was obtained from lidar, a linear trend
689 between the surface pick from the radargram and the surface range from the lidar was calculated, and
690 a resulting slope and offset was used to calculate the theoretical location of the surface. Where

possible, the range-to-ground value was derived from the lidar data or interpolated from the mean lidar elevation within ~700 m. In those rare cases where the surface reflection was picked directly from the radargram, a regression, local to the data gap, was used to fit the radar range to terrain clearance. If lidar was not available to calculate range-to-ground, the height of the aircraft above the surface was obtained by the aircraft's radar altimeter which was then converted into a radar delay time. This conversion was done after a two-stage calibration process which involved recording the terrain clearance over a sea surface with the two instruments, and then correction for the penetration depth of the radar altimeter was obtained from the difference in the height above ellipsoid of a surveyed 'flat' snow surface and the aircraft. Where possible, the reference surface was chosen to be in the centre of the targeted area.

Once bed and surface were calculated, ice thickness was obtained by calculating the difference between the bed and surface pick in range samples (relative to the BAS system). The picked travel time was then converted to depth in metres using a radar wave speed of 168 m/microseconds and a constant firn correction of 10 m. Bed and surface elevations were then integrated with a high-precision kinematic dual-frequency GPS position solution to provide the final point dataset of elevations relative to the WGS84 Ellipsoid. To ensure best accuracy of satellite-orbit definitions and atmospheric corrections, the interpolated survey locations and aircraft elevations were processed from 10-Hz coupled Precise Point Positioning (PPP) GNSS/INS solutions one month after data acquisition.

4. FAIR Data Publishing

In total, we have published 64 datasets from 24 surveys as part of this data release, representing ~566 GB of data and ~1800 files. This amounts to a total of 3.62 million gravity and 7.41 million magnetic data points, as well as 14.5 million ice-thickness and bed-elevation measurements. The complete list of published datasets is provided in Table 3, including the short Digital Object Identifiers (DOI), which redirect to the metadata sheets and download folders for each respective dataset archived on the PDC Discovery Metadata System (DMS) data catalogue (https://data.bas.ac.uk/).

Table 3. Short Digital Object Identifiers for the gravity, magnetic, bed-pick, and 2-D radar datasets for each survey flown by BAS and included in this data release. Abbreviations used are the same as in Table 1. The links in this table can also be accessed by adding the short DOI preceded by 'https://doi.org/'. [1] For the AGAP radar data, the US-led survey lines can be found at: https://doi.org/10.1594/IEDA/313685. [2] For the PolarGAP survey, data can be downloaded from both the ESA and BAS data catalogues, but the DOI for the gravity and magnetic data (https://doi.org/10.5270/esa-8ffoo3e) belongs to ESA. If using the PDC data catalogue, the PolarGAP gravity and magnetic data can be downloaded from https://data.bas.ac.uk/full-record.php?id=GB/NERC/BAS/PDC/01583 and https://data.bas.ac.uk/full-record.php?id=GB/NERC/BAS/PDC/01584 respectively. "**" indicates that the data are not held at BAS, but instead are available on the CReSIS data portal (https://data.cresis.ku.edu/).

Survey	Year	Region	Gravity	Magnetic	Bed-pick	Radar
EVANS	1994-95	WAIS	10/d549	-	10/d548	-
Black Coast	1996-97	APIS	-	10/d54x	-	-
CHARCOT	1996-97	APIS	-	10/d54z	-	-
JRI	1997-98	APIS	10/d55g	10/d55f	-	-
LARSEN	1997-98	APIS	-	10/d55k	-	-
DUFEK	1998-99	WAIS	10/d546	10/d544	10/d542	-
AFI Coats Land	2001-02	EAIS	-	10/dpnw	10/dpnx	-
MAMOG	2001-02	EAIS	10/dpqg	10/dpqh	10/dpqd	-
TORUS	2001-02	WAIS	10/dpqm	10/dpqj	10/dpqf	-

SPARC	2002-03	APIS	10/d552	10/d55x	-	-
BBAS	2004-05	WAIS	10/dpn6	10/dpn3	10/dpnz	10/gzqs
WISE-ISODYN	2005-06	EAIS	10/d554	10/d553	10/cncc	10/gzqq
GRADES-IMAGE	2006-07	WAIS	-	10/d55d	10/d55c	10/gzqj
AGAP	2007-09	EAIS	10/dpnf	10/dpnn	10/dpnr	10/gzqw [1]
ANDRILL HRAM	2008-09	WAIS	-	10/d54w	-	-
Adelaide Island	2010-11	APIS	-	10/dn8b	-	-
IMAFI	2010-11	WAIS	10/dn8g	10/dn8h	10/dn8f	10/gzqr
PIG Ice Shelf	2010-11	WAIS	-	10/d55m	10/d55n	-
ICEGRAV	2011-13	EAIS	10/dpqb	10/dpp9	10/cjzn	10/gzqt
FISS 2015	2015-16	WAIS	-	10/g36h	10/g35q	10/g35m
PolarGAP	2015-16	EAIS	10/g7kw [2]	10/g7kw [2]	10/g7qq	10/g7qp
FISS 2016	2016-17	WAIS	10/g36f	10/g36j	10/g35t	10/g35p
ITGC 2018	2018-19	WAIS	10/dn26	10/dn24	**	**
ITGC 2019	2019-20	WAIS	10/g68r	10/g68q	10/gp4z	10/g7qn

728

We note that individual profiles opportunistically acquired following larger aerogeophysical surveys (i.e. flightlines over Flask Glacier; Farinotti et al., 2013) are not included in this data release unless specifically mentioned in the metadata for each survey (see Table 3). Such small-scale datasets will be added to the data portal in future releases.

Below, we discuss the release of the datasets centered around the four FAIR data principles (i.e. Findable, Accessible, Interoperable and Re-Usable; Wilkinson et al., 2016), starting with the formats and attributes used to store and describe the data (Interoperability; Sect. 4.1), the metadata and Digital Object Identifiers assigned to each dataset (Findability; Sect. 4.2), the data-portal interface and functionalities (Accessibility; Sect. 4.3), and finally the creation of a user guide and open-access tutorials written in Python and MATLAB for reading the data programmatically (Re-usability; Sect. 4.4).

4.1. Interoperability: Data Formats and Attributes

In order to make our data as interoperable as possible, the choice of an open format for all our datasets was a priority. We followed the best practices of the geophysics community and used common data formats and naming conventions to describe the variable names. These are detailed further here.

The gravity, magnetic, and bed-pick data are stored in open ASCII data formats, namely XYZ and CSV files, to ensure long-term access and unresctricted use of the data in the future (Fig. 4). Additionally, we followed the SCAR ADMAP2 data-release protocols (Golynsky et al., 2018) for the naming convention of the channels for the magnetic data. For the radar data, we chose to release the bed-pick data separately from the full radar data (Fig. 4), although the full radar product contains most of the information stored in the ASCII bed-pick files. Publishing the bed-pick data separately from the radar data was a deliberate choice: it alleviates the need for users to download the full radar datasets to access light-weight tabular data, and improves the accessibility of the point data for large gridded products such as SCAR's BEDMAP (Fretwell et al., 2013) and NASA's BedMachine (Morlighem et al., 2020) projects. The bed-pick data are stored as ASCII-formatted files (namely XYZ and CSV), whereas the full radar data are stored as SEG-Y and NetCDF files, reasons for which are described below.

The SEG-Y format has been used extensively by radar scientists since the early 1980s to store radar data. This is primarily due to the lack of a radar-specific format, SEG-Y having been developed primarily to store seismic data. The advantage of using SEG-Y files is that data can be readily

760 imported into seismic-interpretation software for data interpretation and analysis. The drawbacks of
761 using SEG-Y, however, are numerous, making this option unsuitable for long-term data storage.
762 These include: (1) limited space for metadata, (2) the choice of byte-information to store the radar
763 data is subjective due to the nature of the SEG-Y format, (3) until recently, the byte stream structure
764 which includes the geolocation of each radar trace (i.e. the X and Y positions) was restricted to integer
765 format leading to large inaccuracies in the actual trace position despite the use of high-resolution, sub-
766 metre GPS data (see Section 3.1.4). Recognising, however, the need from the geophysical community
767 to view and analyse the radar data in conventional data formats, we have decided to continue
768 producing SEG-Y files for each flightline and acquisition mode (e.g. pulse and chirp). The SEG-Y
769 files were produced using the Revision 1.0 SEG-Y format and georeferenced using the navigational
770 position of each trace from the GPS on board the aircraft in Polar Stereographic (EPSG: 3031)
771 projection. Each SEG-Y file contains the following byte-information: trace number (byte: 1-4 and 5-
772 8), PRI-Number (byte: 9-12), Cartesian X-coordinate (byte: 73-76), Cartesian Y-coordinate (byte: 77-
773 80), number of samples for each SEG-Y trace (byte: 115-116), and the sampling interval (byte: 117-
774 118).

775 As a result of the issues mentioned above, we also exported and published the radar data in
776 NetCDF-formatted files. We chose the NetCDF format due to its portability and array-oriented
777 structure, the ability to store large amounts of metadata and variables into one portable file, its
778 machine-readable capability, and to harmonise our data products with other fields such as climate
779 science (e.g. ECMWF ERA5 reanalysis products; NCAR climate data), glaciology (e.g. Le Brocq et
780 al., 2010; Morlighem et al., 2017; Lei et al., 2021) and, increasingly, radar geophysics itself (e.g.
781 Paden et al., 2014; Blankenship et al., 2017), which already all make use of this data format
782 effectively. The NetCDF files we produced contain extensive metadata relating to the acquisition and
783 processing of the radar data, as well as a set of CF-compliant (Climate and Forecast;
784 https://cfconventions.org/) variables that are tied to the radar data (Table 4). As a minimum, each
785 NetCDF file contains a radar data variable (one for the pulse and/or one for the chirp if both exist) in
786 2-D format, and a set of 1-D variables relating directly to the radar data, such as the trace number, PRI
787 number, fast time, and the X and Y coordinates (Table 4). We also provided additional radar-related
788 variables which were extracted from the radar data following processing, such as the surface and bed
789 picks, the surface and bed elevation, the ice thickness, longitude and latitude, time of the trace, and
790 the elevation of the aircraft (Table 4). Additional 1-D variables include the source of the surface pick
791 (from lidar or radar) if this exists, the range between the aircraft and the ice surface, and in case the
792 pulse- and chirp-radar variables do not have the same length, we provide two sets of variables for the
793 trace number and PRI number.

794 **Table 4. Attributes for each variable stored in the NetCDF files.** For each attribute name, we
795 provide the long name, the dimension (1- or 2-D, x- or y-axis), the short or CF-compliant standard name, and
796 the unit of the measurement. The standard name is only provided if it exists as part of the CF convention
797 (https://cfconventions.org/), otherwise a short name is provided. "dBm" stands for decibel-milliwatts and "a.s.l."
798 stands for above sea level. Note that the surface and bed pick data are referenced to the sampling time of the
799 BAS radar systems across the 64 microseconds pulse repetition interval window, and digitised according to the
800 receiver sampling frequency (see Table 2).

NetCDF Attributes	Long Name	Dimension	Short / Standard Name	Unit
traces	Trace number for the radar data	1-D (x-axis)	traceNum	integer count (unitless)
fast_time	Two-way travel time	1-D (y-axis)	time	microseconds
x_coordinates	Cartesian x-coordinates for the radar data	1-D (x-axis)	projection_x_coordinate	meters (WGS84 EPSG: 3031)

y_coordinates	Cartesian y-coordinates for the radar data	1-D (x-axis)	projection_y_coordinate	meters (WGS84 EPSG: 3031)
chirp_data	Radar data for the processed chirp	2-D (x- and y-axis)	-	power (dBm)
pulse_data	Radar data for the processed pulse	2-D (x- and y-axis)	-	power (dBm)
longitude_layerData	Longitudinal position of the trace number	1-D (x-axis)	longitude	degree_east (WGS84 EPSG: 4326)
latitude_layerData	Latitudinal position of the trace number	1-D (x-axis)	latitude	degree_north (WGS84 EPSG: 4326)
UTC_time_layerData	Coordinated Universal Time (UTC) of trace number	1-D (x-axis)	resTime	seconds of the day
PriNumber_layerData	Incremental integer reference number related to initialisation of the radar system	1-D (x-axis)	PriNum	integer count (unitless)
terrainClearance_layerData	Terrain clearance distance from platform to air interface with ice, sea or ground	1-D (x-axis)	resHt	meters
aircraft_altitude_layerData	Aircraft altitude	1-D (x-axis)	Eht	meters a.s.l. (WGS84 ellipsoid)
surface_altitude_layerData	Ice surface elevation for the trace number	1-D (x-axis)	surface_altitude	meters a.s.l. (WGS84 ellipsoid)
surface_pick_layerData	Location down trace of surface pick (BAS system)	1-D (x-axis)	surfPickLoc	time sample (microseconds)
bed_altitude_layerData	Bedrock elevation for the trace number	1-D (x-axis)	bed_altitude	meters a.s.l. (WGS84 ellipsoid)
bed_pick_layerData	Location down trace of bed pick (BAS system)	1-D (x-axis)	bedPickLoc	time sample (microseconds)
land_ice_thickness_layerData	Ice thickness for the trace number	1-D (x-axis)	land_ice_thickness	meters

801

802   Lastly, to aid visualisation and improve efficiency in navigating the datasets, we created
803 lightweight quick-look PDF files of the radar data for each flightline of each survey (see example for
804 the WISE-ISODYN survey in Figure 7). The choice of ~25 or ~50-km length for the 2-D radargram
805 was chosen based on clarity of the image and varies from survey to survey. The quick-look PDF files
806 are stored alongside the SEG-Y and NetCDF files and are accessible using the links provided in Table
807 3.
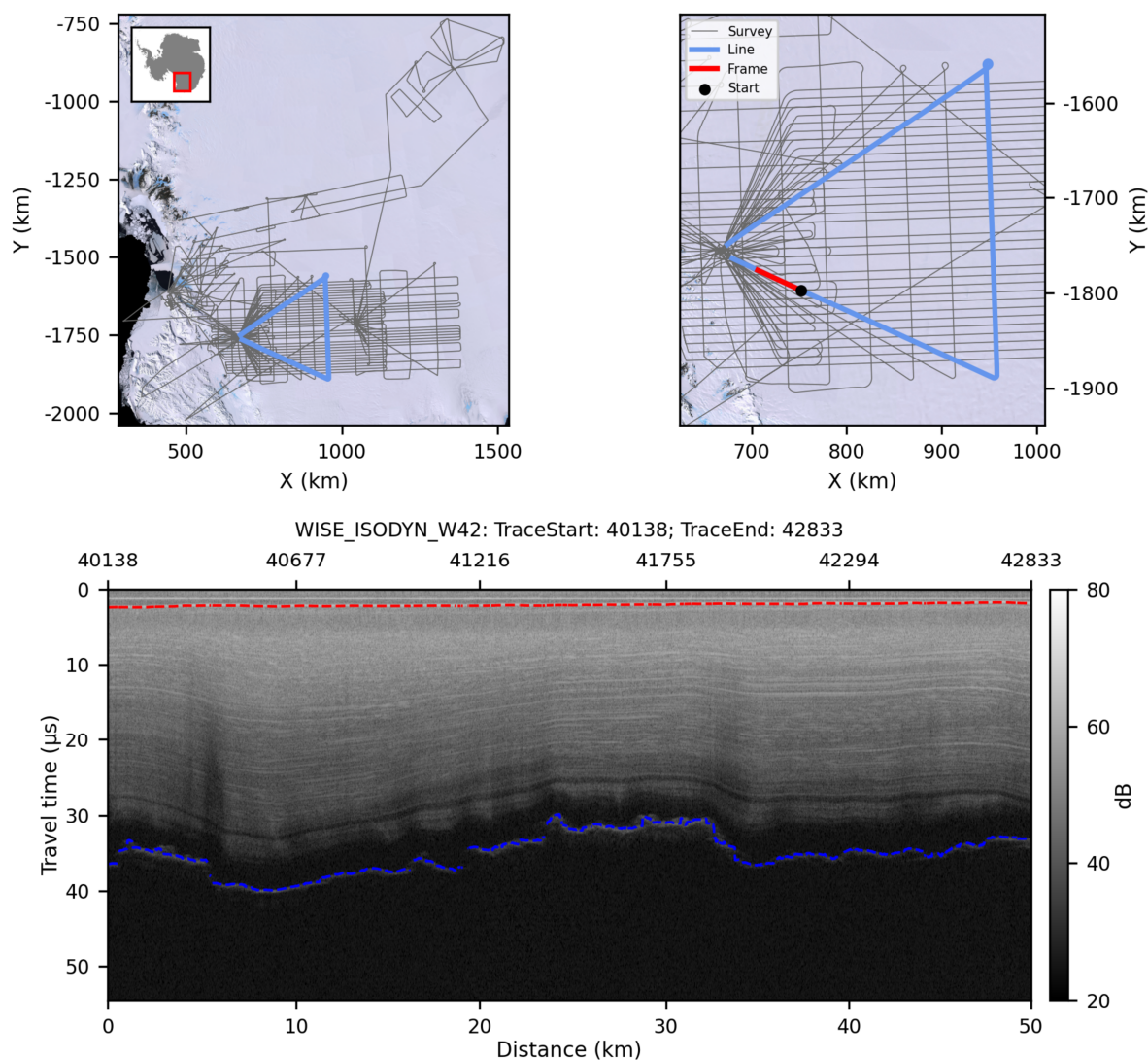
Figure 7. Example of a segmented quick-look image from the 2005-06 WISE-ISODYN survey. (a) Overview map of the survey flightlines (grey lines) with an inset over Antarctica and the specific flightline highlighted in blue. (b) Zoom-in version of (a) showing the specific flightline with the footprint of the 50-km segment (red line) and start point for the radargram (black dot) shown in (c). The background satellite image in (a-b) is from the Landsat Image Mosaic of Antarctica (LIMA) (Bindschadler et al., 2008). (c) 50-km segmented radar image of the chirp data with distance in kilometres shown in the bottom x-axis and the trace number shown in the top x-axis. The y-axis shows the travel time in microseconds. The format of the title in (c) is as follows: Survey Name and Flight ID, First Trace of Segment, Last Trace of Segment. The red and blue dashed lines on the radargram in (c) show the surface and bed pick respectively.

4.2. Findability: Metadata and Digital Object Identifiers

ISO 19115/19139 Geographic Information metadata are provided for each data type of each survey and is archived alongside the datasets onto the PDC DMS catalogue (https://data.bas.ac.uk/; see Table 3). Each metadata record provides detailed information about the dataset, including an abstract, list of personnel involved in the acquisition or analysis of the dataset, and detailed lineage information on the acquisition and processing steps used to produce the dataset amongst others. All our data are covered under the UK Open Government License (http://www.nationalarchives.gov.uk/doc/open-government-licence/), enabling the re-use of the data freely and with flexibility, whilst at the same time ensuring acknowledgment of those involved in the

827 collection and processing of the data. In addition, we use Earth Science-specific keywords and
828 vocabularies from the Global Change Master Directory (GCMD, 2021) to describe our data in a
829 consistent and comprehensive manner in accordance with ISO 19115 standards. Lastly, a Digital
830 Object Identifier is minted for each dataset so that it can be discoverable and adequately cited. The
831 end goal is to provide all the information necessary for effective, long-term data re-use.

832 The data are shared via the web-based RAMADDA (Repository for Archiving and MAnaging
833 Diverse DAta; https://geodesystems.com/) data repository system which is an open-source content
834 and data management platform. The download of the data is done through a standard HTTP-protocol
835 where no login account is required. In the backend, the data are stored following a simple folder
836 structure on the PDC server that is mirrored onto RAMADDA. This simple structure allows us to
837 maintain a balance between the services we can provide and our ability to move away from specific
838 tools – RAMADDA in this case - and potentially adopt more performant systems in the future. The
839 goal is to stay as independent of the platform we use as possible while providing the most effective
840 service possible.

841 **4.3. Accessibility: Polar Airborne Geophysics Data Portal**

842 To increase the accessibility and discoverability of our data, we developed a new data portal,
843 the Polar Airborne Geophysics Data Portal (https://www.bas.ac.uk/project/nagdp/). The portal
844 interactively showcases the wide coverage of aerogeophysical datasets collected by BAS and enables
845 users to easily discover and download the published datasets via a series of widgets and functionalities
846 aimed at enhancing the user experience.

847 The portal is divided into five layer-menus: "Aerogravity", "Aeromagnetics", "AeroRadar",
848 "Boundaries & Features", and "Basemaps". The first three menus contain shapefile layers for the
849 gravity, magnetic, and radar datasets respectively. The "Boundaries & Features" menu contains a set
850 of specific boundary layers, such as the Antarctic Coastline and Ice Drainage boundaries amongst
851 others, and the "Basemaps" menu contains background gridded maps of ice thickness, surface and bed
852 elevations, magnetic anomaly and geothermal heat flow amongst others.

853 The track lines for each dataset correspond to individual polyline shapefiles (either segmented
854 in 25 or 50-km, or by flightline) which contain key statistics such as the minimum, maximum, and
855 median gravity and magnetic anomalies, and minimum, maximum, and median ice surface, bed
856 elevation, and ice thickness. The shapefiles also contain direct links to the survey's metadata and to
857 direct links to download the data via the RAMADDA interface.

858 A powerful functionality of the portal is the ability to view the aerogeophysical data rapidly
859 via the creation of quick-look gravity, magnetic, and radar plots for each flightlines (see Section 5.2;
860 Figure 7c). For the magnetic and gravity data, graphs showing the magnetic or free-air anomaly along
861 straight lines were created in the direction Westernmost-Easternmost if the profile is mainly in the
862 direction of the longitude, or Northernmost-Southernmost if the profile is predominantly in the
863 direction of the latitude. For the radar data, the segmented images were produced in a similar format
864 to Figure 7c and split into ~25 and~50 km segments depending on the survey.

865

4.4. Re-Usability: User Guide and Tutorials

To increase further the re-usability of our data, we provided a user guide for the data portal as well as interactive, open-source Jupyter Notebook tutorials written in Python and MATLAB for reading in the gravity, magnetic, and radar datasets and conducting first-order analyses on the data. These are archived on the BAS GitHub repository and provided via an interactive web interface using Jupyter Book (https://antarctica.github.io/PDC_GeophysicsBook). We believe these to be particularly beneficial for ensuring accessibility and re-usability of our data to as wide of a range of users as possible, primarily as a result of the complexity around reading in aerogeophysical data formats.

5. Discussion

This final section exemplifies the potential re-usability of the newly released aerogeophysical data via the interrogation of the englacial architecture of the ice as sounded by BAS ice-penetrating radars. We also explore the future use of the new data portal and discuss opportunities in terms of data release and further potential re-use of the BAS aerogeophysical data.

5.1. Internal Layering Continuity Index

Englacial layering, as imaged by ice-penetrating radars, is a powerful means of extracting information on past ice-dynamical processes (Rippin et al., 2003b; Siegert et al., 2003; Bingham et al., 2015) amongst others. For example, the presence of well-preserved and continuous englacial layering may reflect stable ice conditions and suggest limited changes in past ice-flow conditions, ice divide migration, or melting within or at the base of an ice sheet (Karlsson et al., 2012). In contrast, poor continuity in englacial layering, primarily characterised by buckled or absent layering, may be indicative of past ice-flow switching or increased englacial stress gradients (Siegert et al., 2003; Bingham et al., 2015).

The Internal Layer Continuity Index (or ILCI; Karlsson et al., 2012) provides an automated tool for quantitatively assessing the continuity of englacial layering based on A-scope radar profiles. This method has the advantage of being much less laborious than manual methods (e.g. Rippin et al., 2003a; Siegert et al., 2003; Bingham et al. 2007) and removes the potential subjectivity in assessing layer continuity. By design, the ILCI is sensitive to the number and strength of internal reflections, such that low values indicate discontinuity and high values indicate high continuity. Whilst the ILCI has previously been calculated over individual surveys (Karlsson et al., 2012; Bingham et al., 2015; Winter et al., 2015; Karlsson et al., 2018; Luo et al., 2020), until now, this approach had not been tested at a regional scale over Antarctica and with the use of multiple radar datasets. Enabled by the comprehensive release of large swaths of fully standardised and open-access aerogeophysical data described in this paper, we aim to demonstrate that much more information can be extracted from these data on a regional- to continental-scale, which would not have otherwise been possible before.

Here, we have calculated the ILCI on the ten PASIN radar datasets acquired between 2004-2020 that have been published as part of this data release (see Table 3; Figure 8-9); and which amount to ~300,00 line-km of data. Since we were primarily interested in regional changes in layer continuity, the ILCI was smoothed using a horizontal window of 1,000 samples (representing ~25-45 km distance depending on the dataset) to remove any small-scale anomalies in the data and only making use of the deep-sounding chirp product due to its capability of imaging deeper internal layers. The upper and lower 20% of the ice were also omitted in the calculations due to the inability of the PASIN system to resolve continuous layers in the upper portion of the ice column, and because internal layering is typically absent near the ice-bed interface (Drews et al., 2009; Karlsson et al., 2012).

909
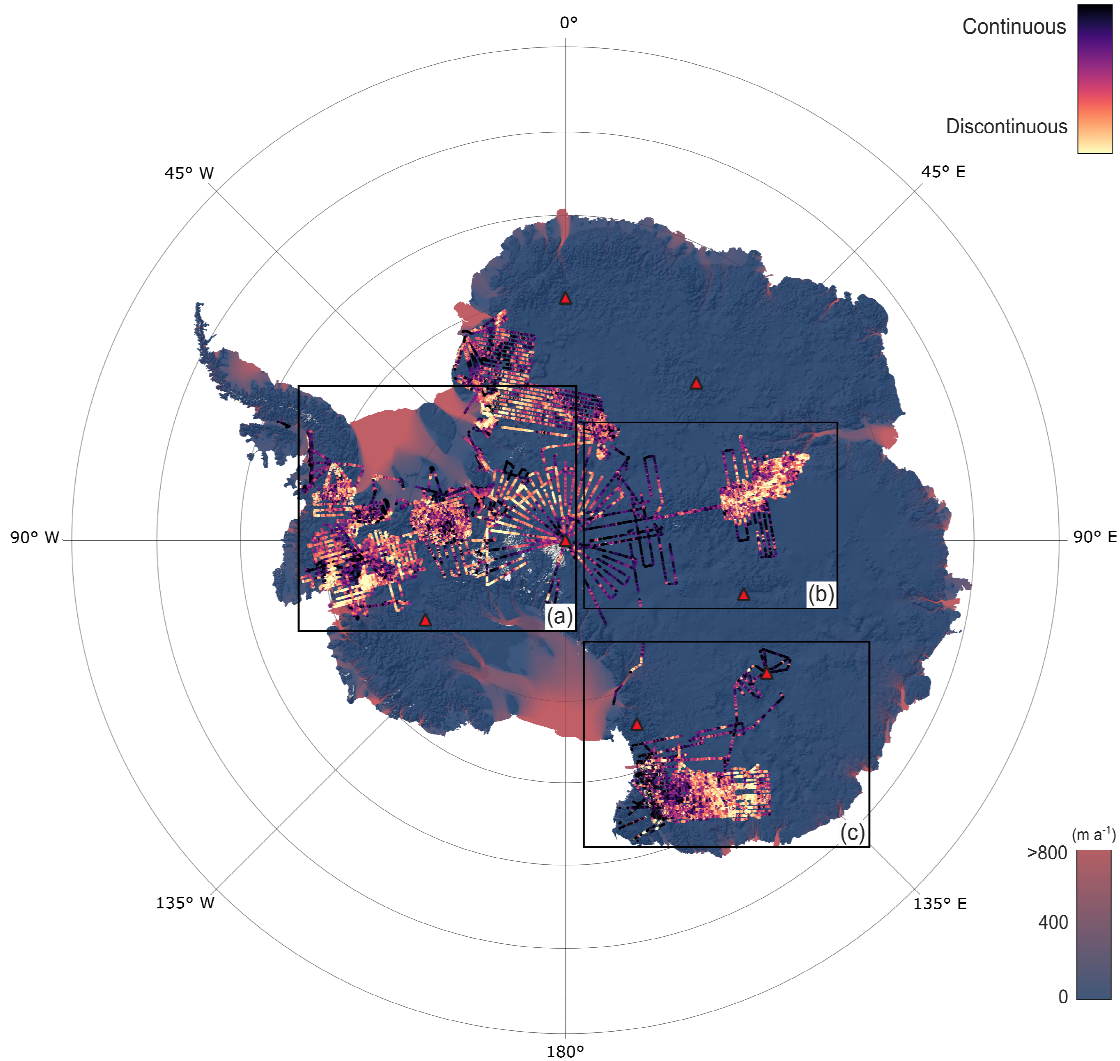
Figure 8. Internal Layer Continuity Index for the ten PASIN datasets for which the fully
processed 2-D radar data was released as part of this paper (see Table 3). The background map shows ice-
flow velocities from the In-SAR MEaSUREs dataset (Rignot et al., 2017) superimposed over a hill-shade from
the BedMachine bed elevation V2 dataset (Morlighem, 2020). The red and blue colour bar shows ice-flow
velocities in metres per annum, and the magma colour bar shows the continuity of internal layers throughout the
radar dataset (low continuity = yellow; high continuity = dark purple). The black-bordered rectangles (a-c)
correspond to the close-up plots in Figure 9a-c. The red triangles correspond to existing deep ice-cores located
near the BAS radar surveys.

An important consideration in employing the ILCI over multiple datasets is that the results
will vary based on data acquisition (i.e. radar frequency, system resolution) and processing applied
(i.e. incoherent vs 2-D SAR), thus a pan-Antarctic comparison of internal layer continuity must be
analysed in this context. This is especially the case here, where we have applied the ILCI to data
acquired over a period of >15 years with two different systems (namely PASIN-1 and PASIN-2) and
using different processing regimes. Therefore, care must be taken when interpreting the results from
different surveys together, as for example, a low level of layer continuity in the main trunk of Pine
Island Glacier on the BBAS survey may not reflect the same level of discontinuity on the low-
continuity areas of the PolarGAP survey. This caution noted, the results presented here offer an
opportunity to identify some regional patterns of potential value for future work, which we now
discuss.

929   Figure 8 shows that there is a good correspondence between discontinuous layering where ice
930   flow is fast (> 200 m a^{-1}) such as over Foundation Ice Stream (FISS) and the main trunk of Pine Island
931   Glacier (BBAS) and Slessor Glacier (ICEGRAV) (Fig. 8 and 9a). Whilst layer discontinuity is mainly
932   present over the WAIS due to the high concentration of fast-flowing ice streams in this region, several
933   sections covering the EAIS also show signs of layer discontinuity, particularly in the upstream
934   portions of the fast-flowing Lambert Glacier (AGAP) and David and Ninnis glaciers (WISE-
935   ISODYN) (yellow arrows in Fig. 9b-c).

936   Unsurprisingly, areas of high continuity are mainly observed over the interior of the EAIS,
937   particularly on flightlines extending deep into East Antarctica and South Pole (Fig. 8 and 9a-b), as
938   well as into the deeper parts of the Wilkes Subglacial Basin and Dome C (black arrow in Fig. 9c)
939   where deep ice-cores have been drilled (red triangles in Fig. 8-9). Areas of high layer continuity over
940   the WAIS include numerous ice-rises (i.e. Bungenstock, Fletcher, Henry, and Korff) as imaged on the
941   GRADES-IMAGE, IMAFI, and FISS surveys (black arrows in Fig. 9a), the deeper sections of the
942   southern Pine Island Glacier basin on the BBAS data, as well as on PolarGAP survey lines upstream
943   of the FISS grids covering Foundation Ice Stream and Recover and Slessor glaciers (Fig. 9a).

944   Also visible are the disruptive effects of local bed topography on the continuity of internal
945   layering, such as over the Ellsworth Subglacial Highlands (BBAS), the Transantarctic Mountains
946   (IMAFI and PolarGAP), and the Gamburtsev Subglacial Mountains (AGAP) (see yellow arrows in
947   Fig. 9a-b), whereas relatively flat bed topography in the deep interior of the EAIS allow layering to
948   remain relatively undisturbed there (Fig. 8 and black arrows in Fig. 9b).
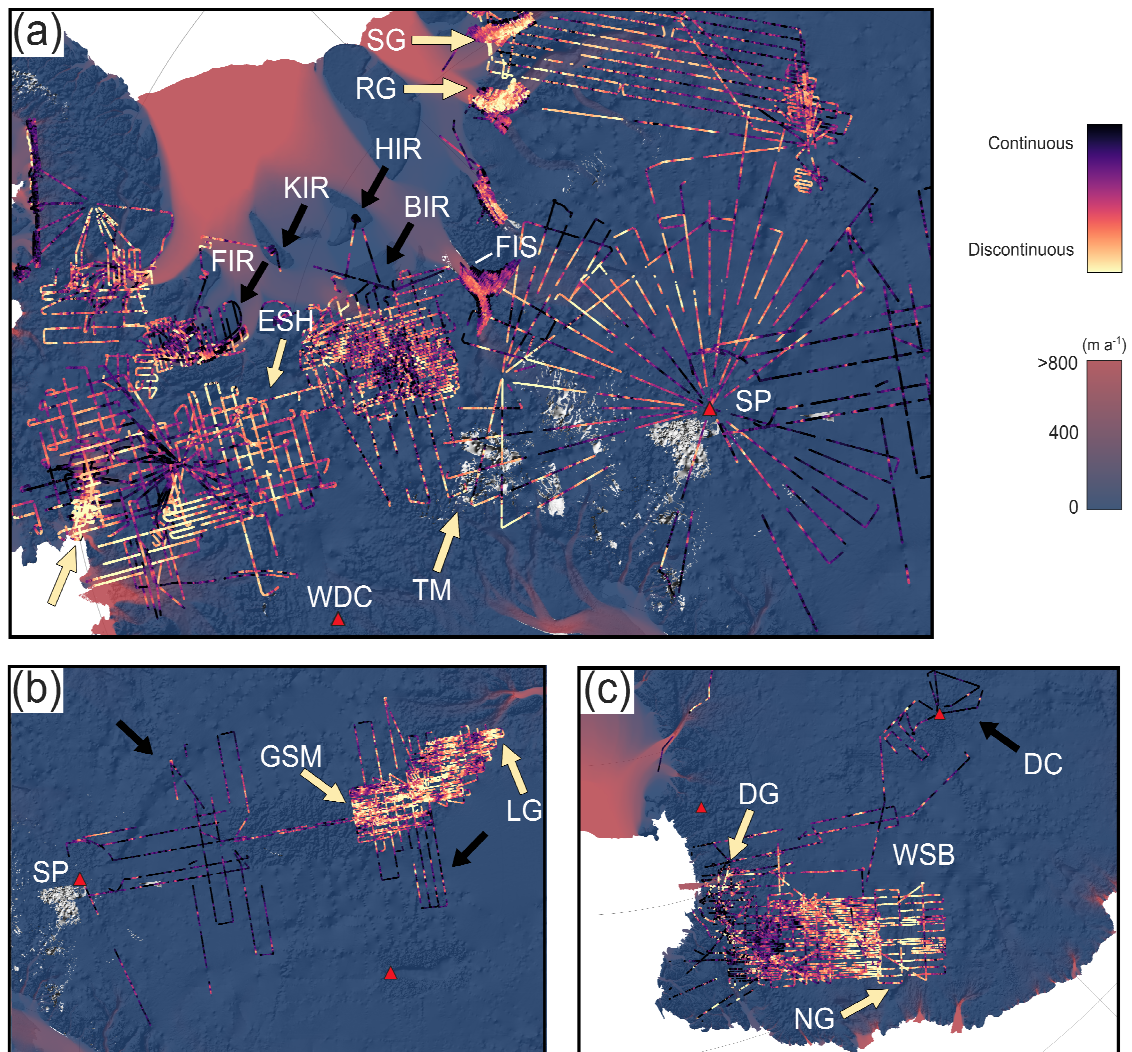
Figure 9. Zoomed-in sections of the Internal Layer Continuity Index shown in the black-bordered rectangles on Figure 8. The basemap datasets and colour scales are the same as in Figure 8. (a) ILCI results over the WAIS (including Pine Island Glacier, Rutford Ice Stream, Institute-Möller Ice Stream, and Foundation Ice Stream) and bottleneck with the EAIS (including South Pole, Pensacola Mountains and Slessor Glacier), (b) ILCI results for the AGAP survey over East Antarctica's Dome A and South Pole, (c) ILCI results for the WISE-ISODYN survey over East Antarctica's Wilkes Subglacial Basin and Dome C. Arrows refer to locations mentioned in the text, with black arrows highlighting examples of high layer continuity and yellow arrows low layer continuity. As per Figure 8, the red triangles correspond to existing deep ice-cores located near the BAS radar surveys. Abbreviations correspond to locations mentioned in the text, as follows: BIR (Bungenstock Ice Rise); DC (Dome C); DG (David Glacier); ESH (Ellsworth Subglacial Highlands); FIR (Filchner Ice Rise); FIS (Foundation Ice Stream); GSM (Gamburtsev Subglacial Mountains); HIR (Henry Ice Rise); KIR (Korff Ice Rise); LG (Lambert Glacier); NG (Ninnis Glacier); RG (Recovery Glacier); SG (Slessor Glacier); SP (South Pole); TM (Transantarctic Mountains); WDC (WAIS Divide Core); WSB (Wilkes Subglacial Basin).

Altogether, the results presented in Figures 8 and 9 show considerable promise for those radar datasets to be exploited further in the future, particularly with regards to tracking or otherwise characterising the englacial architecture of the ice and as motivated by the SCAR AntArchitecture group. At present, only two BAS radar datasets (BBAS and IMAFI) have been comprehensively assessed for deep englacial layers (Karlsson et al., 2009; Ashmore et al., 2020; Ross et al., 2020; Bodart et al., 2021). Importantly, the close proximity of deep ice cores, such as the WAIS Divide (Buizert et al., 2015; Sigl et al., 2016), EPICA Dome C (EPICA Community Members, 2004), and

971 South Pole (Winski et al., 2019), to these newly released surveys (Fig. 8-9) provide ready
972 opportunities for these layers to be dated, increasing significantly their wider use for glaciological and
973 geophysical applications (i.e. Siegert and Payne, 2004; Parrenin and Hindmarsh, 2007; Cavitte et al.,
974 2018; Sutter et al., 2021).

975 **5.2. Polar Airborne Geophysics Data Portal**

976 One specificity of the platform is that it offers three types of geophysical datasets - namely
977 gravity, magnetic and radar - at the same time geospatially. Although some surveys were acquired
978 over 25 years ago, they may never have been exploited or analysed fully in a form that reached peer-
979 reviewed publications, nor combined with other geophysical data before, increasing in turn their re-
980 usability. By publishing this resource, we anticipate that the portal and datasets will foster new
981 research and discoveries related to our understanding of ice-sheet processes and crust and lithosphere
982 heterogeneity beneath the Antarctic Ice Sheet.

983 Additionally, the portal enables users to combine the published line datasets with gridded
984 products to compare the ability of the interpolated datasets to match the direct observations. For
985 instance, as shown in Figure 10 for the 2012-13 ICEGRAV survey, the portal allows users to readily
986 investigate the free-air gravity anomaly with the bed topography from BEDMAP2 or assess the
987 consistency between the measured ICEGRAV magnetic anomalies and the gridded aeromagnetic
988 product (Fig. 10). Alternatively, the quick-look radargrams can be compared with the ice-thickness
989 and bed-elevation grid cells from BEDMAP to assess sub-km variations in along- and across-flow on
990 the radar data which may have been smoothed out in the 1-km gridded product.

991 With its ~207,000 line-km of gravity, ~338,000 line-km of magnetic, and ~352,000 line-km
992 of radar data published, the Polar Airborne Geophysics Data Portal provides a robust platform for the
993 dissemination of the BAS aerogeophysical data. Further opportunities offered by the data portal are
994 the potential for the platform to be used to plan future field surveys or encourage future compilation
995 efforts based on gaps in the data coverage or quality of the data.
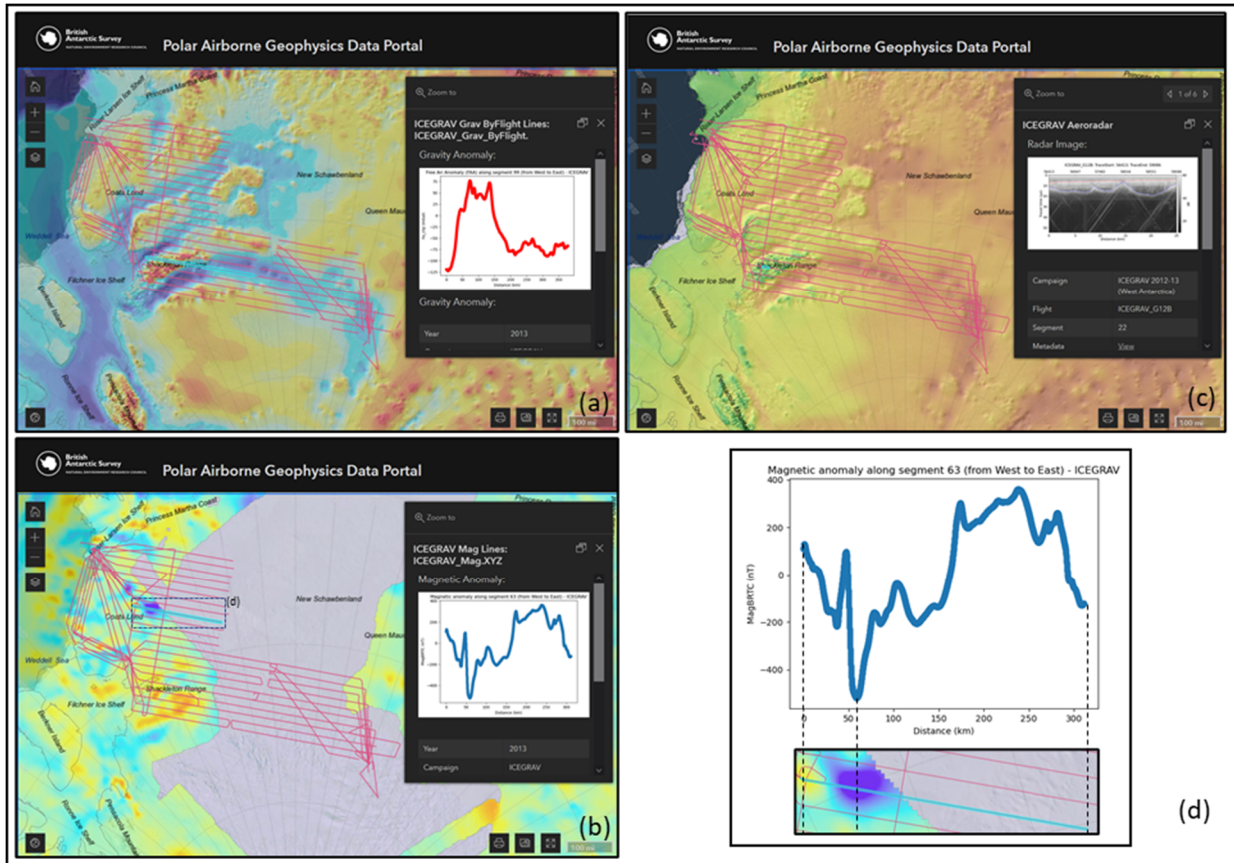
Figure 10. Screenshots of the Polar Airborne Geophysics Data Portal showing the three aerogeophysical products for the 2012-13 ICEGRAV survey with different basemaps. (a) ICEGRAV aerogravity survey with the BEDMAP2 bed elevation basemap (b) ICEGRAV aeromagnetic survey with the magnetic anomaly basemap from Goodge and Finn (2010), (c) ICEGRAV aeroradar survey with the ice thickness basemap from BEDMAP2. (d) Magnetic anomaly along the profile highlighted in (c) with a comparison with the aeromagnetic anomaly map from Goodge and Finn (2010).

5.3. Future Work

Although most of data published here have already been incorporated into previous data compilations such as BEDMAP2 or ADMAP2, the more recent datasets presented here will provide useful additions to future editions of such initiatives. Examples of this are the data acquired as part of the 2012-13 ICEGRAV aeromagnetic campaign in Dronning Maud Land where the last compilation effort of magnetic anomalies had shown a large gap (Goodge and Finn, 2010; Fig. 10), or the new ice-thickness and bed-elevation data acquired over Thwaites Glacier (2018-20), South Pole (2015-16), and Filchner Ice Shelf (2015-17) which are expected to be added to the new BEDMAP3 compilation.

Even though most of the gravity, magnetic and bed-pick data acquired since the mid-1990s are now fully published, radar data from older surveys (1994-2004) for which the bed-pick data are published and already integrated into larger gridded products (e.g. BEDMAP; Fretwell et al., 2013) are yet to be published in full as per the more modern surveys (2004-2020) released here (see Table 3). This is primarily due to poorer data management practices at times of acquisition and less well-documented processing procedures which restrict the re-usability of these older radar dataset. Much older analogue radar data acquired on films and video tapes prior to the deployment of digital radars (i.e. pre-1994) also offer additional opportunities, although the necessity for manual digitisation makes this task much more time consuming and challenging. It is worth noting, however, that many of the regions broadly covered by these older surveys have recently been re-flown using more modern

1022 instruments, much as part of NASA's Operation IceBridge programme (MacGregor et al., 2021),
1023 although reprocessing and modernising older radar data can bring substantial benefits, as already
1024 demonstrated by Schroeder et al. (2019). Additional reprocessing of older radar data using modern 2-
1025 D SAR techniques would also be beneficial, as recently demonstrated on BAS data (see Castelletti et
1026 al., 2020; Chu et al., 2021).

1027 As a result of the very flexible configuration of the PASIN-2 system, much more data can
1028 also be extracted from the raw radar files already acquired, including fully polarised data used to
1029 image ice crystal-fabric orientation for estimating ice deformation processes (i.e. Young et al., 2021),
1030 or 3-D swath radar data used to reconstruct the sub-surface at finer resolution and without
1031 compromising on across-track resolution as for conventional 2-D data (Holschuh et al., 2020; Arenas-
1032 Pingarron et al., 2022).

1033 Combined, these will likely add further opportunities for future data releases, alongside our
1034 intention to publish newly acquired data regularly via the data portal and following the procedures
1035 detailed in this paper.

6. Conclusion

1037 We have presented here the release of 64 aerogeophysical datasets from 24 surveys flown by
1038 BAS between 1994 and 2020 over the Antarctic Peninsula and East and West Antarctica. Altogether,
1039 the data release consists of ~450,000 line-km (or ~5.3.million km^2) of aerogeophysical data on
1040 gravity, magnetic and radar measurements (including bed-pick from 1994-onwards and the fully
1041 processed 2-D radar data from 2004-onwards) which have all been standardised according to the
1042 FAIR (Findable, Accessible, Interoperable and Re-Usable) data principles. A new data portal, the
1043 Polar Airborne Geophysics Data Portal (https://www.bas.ac.uk/project/nagdp/), and interactive, open-
1044 access tutorials written in Python and MATLAB have also been created to improve the interactivity
1045 and user-accessibility of our datasets.

1046 Aside from discussing the data acquisition and processing steps, we have demonstrated that
1047 much more information can be extracted from the newly released aerogeophysical data by assessing
1048 the continuity of englacial layering along ~300,000 line-km of the ice-penetrating radar data. Using an
1049 automated layer continuity extraction method on all ten fully published 2-D radar datasets, we have
1050 shown that large volumes of radar lines contain well-preserved englacial layering from which further
1051 glaciological and geophysical information could be extracted. We note that the analysis shown in
1052 Section 5.1 is only possible because the data has been comprehensively standardised and made open-
1053 access. Whilst we acknowledge that this type of work may suffer from a lack of funding
1054 opportunities, the results presented here would suggests that re-modernising already acquired data
1055 may be as important as acquiring new data. It also enables their use in emerging fields such as
1056 artificial intelligence, which rely on large amounts of standardised data.

1057 Although all of the datasets released here have so far made a significant contribution to our
1058 understanding of past and current ice-dynamical and lithospheric influences, partly through their
1059 contributions to major international collaborative projects such as the SCAR BEDMAP and ADMAP
1060 programmes, they have until now largely remained unpublished in their full form, thus restricting the
1061 further usage of the data beyond the life cycle of the science projects. It is our hope that these newly
1062 released data will offer further research opportunities and enable the wider scientific community to
1063 benefit from the abundance of newly published aerogeophysical data over Antarctica, particularly
1064 within the context of recently established international projects such as the SCAR AntArchitecture
1065 and RINGS Action groups, the latter of which focuses primarily on fillings gaps in already-acquired
1066 observations at the boundaries of the Antarctic Ice Sheet.

1067 Reflecting on our collaboration between data managers and scientists, we believe that this
1068 project sets a positive example for further release of aerogeophysical data, particularly for future

1069 international initiatives that are aiming to harmonise the availability and findability of
1070 aerogeophysical data collected across Antarctica. A full list of all available datasets can be found in
1071 Table 3 of this paper, or via the BAS Discovery Metadata System (https://data.bas.ac.uk).

Data Availability Statement

1073 All the data included in this manuscript are freely available via the BAS Discovery Metadata System
1074 (https://data.bas.ac.uk), with direct links to the datasets found in Table 3 of this paper. The user guide
1075 for the data portal and the Jupiter Notebook tutorials designed for reading in the gravity, magnetic,
1076 and radar data in Python and MATLAB are freely accessible on the Jupyter Book interface
1077 (https://antarctica.github.io/PDC_GeophysicsBook) or via the BAS GitHub repository
1078 (https://github.com/antarctica/PDC_GeophysicsBook). The code used to produce the Internal Layer
1079 Continuity Index over the whole BAS radar data (Fig. 8-9) is available on the GitHub page of J.A.B.
1080 (https://github.com/julbod).

Competing Interests

1082 The authors declare that they have no conflict of interest.

Contribution Statement

1084 A.C.F. and J.A.B. co-led this data release. A.C.F. initiated the collaboration between the Polar Data
1085 Centre and the BAS Airborne Geophysics science team, with input from H.J.P. A.C.F. quality-
1086 checked and published the gravity, magnetic and bed-pick datasets, with input from T.A.J., F.F, and
1087 J.A.B. J.A.B re-processed, quality-checked, and published the fully processed radar datasets and
1088 accompanying files, with input from A.C.F., T.A.J. and C.R. The three BAS radar systems and
1089 accompanying radar processing software libraries were designed by H.F.J.C. The aerogeophysical
1090 data were primarily acquired and processed by H.F.J.C, C.R., F.F. and T.A.J. J.A.B created the data
1091 portal, with input from A.C.F., T.A.J. and F.F. A.C.F. and J.A.B. populated the data portal with the
1092 gravity, magnetic, and radar track-lines. A.C.F. created the Jupyter Notebook tutorials, with input
1093 from J.A.B. for the radar tutorials and user guide. J.A.B. wrote the code and analysed the results for
1094 the layer continuity index. J.A.B wrote the initial manuscript and created the figures, with input from
1095 A.C.F. All authors commented and contributed to the final edits of the manuscript prior to publication.

Acknowledgments

1097 We would like to thank the many BAS personnel involved over the last three decades in developing
1098 and maintaining the aerogeophysical instruments and in acquiring and processing the data presented
1099 in this paper. In particular, we would like to credit and acknowledge Hugh Corr and Nick Frearson for
1100 designing the PASIN radar systems. We are also especially grateful to the many pilots that flew the
1101 BAS Twin Otter aicraft "VP-FBL" throughout the years, including Lee Proudfoot, Greg Harris, Pete
1102 Buckley, Doug Pearson, Mark Beasley, Doug Cochrane, Andy Vidamour, Oli Smith, and particularly
1103 David Leatherdale and Ian Potten who flew most of the survey km. We would also like to highlight
1104 the scientific contribution of the late Richard Hindmarsh, particularly with regards to the GRADES-
1105 IMAGE survey. Many campaigns that BAS conducted were also in partnership with national and
1106 international collaborators and institutes, which we would also like to acknowledge more widely. We
1107 would also like to acknowledge the help from the BAS PDC and MAGIC (Mapping and GIS) teams
1108 for their valuable input throughout this project. Lastly, the authors thank Neil Ross and an anonymous
1109 reviewer for their constructive suggestions, which improved this manuscript. J.A.B was partly funded
1110 by the NERC Doctoral Training Partnership (grant reference number: NE/L002558/1) hosted in the
1111 Edinburgh E^3 DTP program.

References

1113   Arenas-Pingarron A., Corr H.J.W., Robinson C., Jordan T.A., and Brennan P.V., 2022.
1114 PASIN2, an Ice-Sounding Airborne Synthetic Aperture Radar for Subglacial 3D Imagery. *IET*
1115 *RADAR SONAR NAV.* (In review).

1116

1117   Arndt, J.E., Schenke, H.W., Jakobsson, M., Nitsche, F.O., Buys, G., Goleby, B., Rebesco, M.,
1118 Bohoyo, F., Hong, J., Black, J. and Greku, R., 2013. The International Bathymetric Chart of the
1119 Southern Ocean (IBCSO) Version 1.0—A new bathymetric compilation covering circum-Antarctic
1120 waters. *GEOPHYS RES LETT*, *40*(12), pp.3111-3117. https://doi.org/10.1002/grl.50413

1121

1122   Ashmore, D.W., Bingham, R.G., Hindmarsh, R.C., Corr, H.F. and Joughin, I.R., 2014. The
1123 relationship between sticky spots and radar reflectivity beneath an active West Antarctic ice stream.
1124 *ANN GLACIOL*, 55(67), pp.29-38. https://doi.org/10.3189/2014AoG67A052

1125

1126   Ashmore, D.W. and Bingham, R.G., 2014. Antarctic subglacial hydrology: current knowledge
1127 and future challenges. *ANTARCT SCI*, *26*(6), pp.758-773.
1128 https://doi.org/10.1017/S0954102014000546

1129

1130   Ashmore, D.W., Bingham, R.G., Ross, N., Siegert, M.J., Jordan, T.A. and Mair, D.W., 2020.
1131 Englacial architecture and age-depth constraints across the West Antarctic Ice Sheet. *GEOPHYS RES*
1132 *LETT*, 47(6), p.e2019GL086663. https://doi.org/10.1029/2019GL086663

1133

1134   Bamber, J.L., Ferraccioli, F., Joughin, I., Shepherd, T., Rippin, D.M., Siegert, M.J. and
1135 Vaughan, D.G., 2006. East Antarctic ice stream tributary underlain by major sedimentary basin.
1136 *GEOLOGY*, 34(1), pp.33-36. https://doi.org/10.1130/G22160.1

1137

1138   Becker, D., Nielsen, J.E., Ayres-Sampaio, D., Forsberg, R., Becker, M. and Bastos, L., 2015.
1139 Drift reduction in strapdown airborne gravimetry using a simple thermal correction. *J*
1140 *GEODESY*, *89*(11), pp.1133-1144. https://doi.org/10.1007/s00190-015-0839-8

1141

1142   Bell, R.E., Blankenship, D.D., Finn, C.A., Morse, D.L., Scambos, T.A., Brozena, J.M. and
1143 Hodge, S.M., 1998. Influence of subglacial geology on the onset of a West Antarctic ice stream from
1144 aerogeophysical observations. *NATURE*, *394*(6688), pp.58-62. https://doi.org/10.1038/27883

1145

1146   Bell, R.E., Studinger, M., Fahnestock, M.A. and Shuman, C.A., 2006. Tectonically controlled
1147 subglacial lakes on the flanks of the Gamburtsev Subglacial Mountains, East Antarctica. *GEOPHYS*
1148 *RES LETT*, *33*(2). https://doi.org/10.1029/2005GL025207

1149

1150   Bell, R.E., Ferraccioli, F., Creyts, T.T., Braaten, D., Corr, H., Das, I., Damaske, D., Frearson,
1151 N., Jordan, T., Rose, K. and Studinger, M., 2011. Widespread persistent thickening of the East

Antarctic Ice Sheet by freezing from the base. *SCIENCE*, 331(6024), pp.1592-1595. https://doi.org/10.1126/science.1200109

Bindschadler, R., Vornberger, P., Fleming, A., Fox, A., Mullins, J., Binnie, D., Paulsen, S.J., Granneman, B. and Gorodetzky, D., 2008. The Landsat image mosaic of Antarctica. *REMOTE SENS ENVIRON*, 112(12), pp.4214-4226. https://doi.org/10.1016/j.rse.2008.07.006

Bindschadler, R.A.; Choi, H., Wichlacz, A, Bingham, R., Bohlander, J., Brunt, K., Corr, H., Drews, R., Fricker, H., Hall, M., Hindmarsh, R., Kohler, J., Padman, L., Rack, W., Rotschky, G., Urbini, S., Vornberger, P. and Young, N. (2011) Getting around Antarctica: New high-resolution mappings of the grounded and freely-floating boundaries of the Antarctic ice sheet created for the International Polar Year. *THE CRYOSPHERE*, 5, 569-588. https://doi.org/10.5194/tc-5-569-2011

Bingham, R.G., Siegert, M.J., Young, D.A. and Blankenship, D.D., 2007. Organized flow from the South Pole to the Filchner-Ronne ice shelf: An assessment of balance velocities in interior East Antarctica using radio echo sounding data. *J GEOPHYS RES-EARTH*, *112*(F3). https://doi.org/10.1029/2006JF000556

Bingham, R.G., Ferraccioli, F., King, E.C., Larter, R.D., Pritchard, H.D., Smith, A.M. and Vaughan, D.G., 2012. Inland thinning of West Antarctic Ice Sheet steered along subglacial rifts. *NATURE*, 487(7408), pp.468-471. https://doi.org/10.1038/nature11292

Bingham, R.G., Rippin, D.M., Karlsson, N.B., Corr, H.F., Ferraccioli, F., Jordan, T.A., Le Brocq, A.M., Rose, K.C., Ross, N. and Siegert, M.J., 2015. Ice-flow structure and ice dynamic changes in the Weddell Sea sector of West Antarctica from radar-imaged internal layering. *J GEOPHYS RES-EARTH*, *120*(4), pp.655-670. https://doi.org/10.1002/2014JF003291

Blankenship, D.D., Morse, D.L., Finn, C.A., Bell, R.E., Peters, M.E., Kempf, S.D., Hodge, S.M., Studinger, M., Behrendt, J.C. and Brozena, J.M., 2001. Geologic controls on the initiation of rapid basal motion for West Antarctic ice streams: A geophysical perspective including new airborne radar sounding and laser altimetry results. *THE WEST ANTARCTIC ICE SHEET: BEHAVIOR AND ENVIRONMENT*, *77*, pp.105-121. https://doi.org/10.1029/AR077p0105

Blankenship, D. D., S. D. Kempf, D. A. Young, T. G. Richter, D. M. Schroeder, J. S. Greenbaum, T. van Ommen, R. C. Warner, J. L. Roberts, N. W. Young, E. Lemeur, M. J. Siegert, and J. W. Holt. (2017) *IceBridge HiCARS 1 L1B Time-Tagged Echo Strength Profiles, Version 1*. Boulder, Colorado USA. NASA National Snow and Ice Data Center Distributed Active Archive Center. https://doi.org/10.5067/W2KXX0MYNJ9G

Bodart, J.A., Bingham, R.G., Ashmore, D.W., Karlsson, N.B., Hein, A.S. and Vaughan, D.G., 2021. Age-depth stratigraphy of Pine Island Glacier inferred from airborne radar and ice-core

1193   chronology. *J GEOPHYS RES-EARTH*, 126(4), p.e2020JF005927.
1194   https://doi.org/10.1029/2020JF005927

1195

1196   Bozzo, E. and Ferraccioli, F., 2007. The Italian-British Antarctic geophysical and geological
1197   survey in northern Victoria Land 2005-06-towards the International Polar Year 2007-08.
1198   https://nora.nerc.ac.uk/id/eprint/15403

1199

1200   Buizert, C., Cuffey, K.M., Severinghaus, J.P., Baggenstos, D., Fudge, T.J., Steig, E.J.,
1201   Markle, B.R., Winstrup, M., Rhodes, R.H., Brook, E.J. and Sowers, T.A., 2015. The WAIS Divide
1202   deep ice core WD2014 chronology–Part 1: Methane synchronization (68–31 ka BP) and the gas age–
1203   ice age difference. *CLIM PAST*, *11*(2), pp.153-173. https://doi.org/10.5194/cp-11-153-2015

1204

1205   Castelletti, D., Schroeder, D.M., Mantelli, E. and Hilger, A., 2019. Layer optimized SAR
1206   processing and slope estimation in radar sounder data. *J GLACIOL*, 65(254), pp.983-988.
1207   https://doi.org/10.1017/jog.2019.72

1208

1209   Cavitte, M.G., Parrenin, F., Ritz, C., Young, D.A., Van Liefferinge, B., Blankenship, D.D.,
1210   Frezzotti, M. and Roberts, J.L., 2018. Accumulation patterns around Dome C, East Antarctica, in the
1211   last 73 kyr. *THE CRYOSPHERE*, *12*(4), pp.1401-1414. https://doi.org/10.5194/tc-12-1401-2018

1212

1213   Chu, W., Hilger, A.M., Culberg, R., Schroeder, D.M., Jordan, T.M., Seroussi, H., Young,
1214   D.A., Blankenship, D.D. and Vaughan, D.G., 2021. Multi-system synthesis of radar sounding
1215   observations of the Amundsen Sea sector from the 2004-2005 field season. *J GEOPHYS RES-*
1216   *EARTH*, p.e2021JF006296. https://doi.org/10.1029/2021JF006296

1217

1218   Constantino, R.R., Tinto, K.J., Bell, R.E., Porter, D.F. and Jordan, T.A., 2020. Seafloor depth
1219   of George VI Sound, Antarctic Peninsula, from inversion of aerogravity data. *GEOPHYS RES LETT*,
1220   *47*(21), p.e2020GL088654. https://doi.org/10.1029/2020GL088654

1221

1222   Corr, H. and Popple, M., 1994. Airborne radio echo sounding on the Evans flowline, Ronne
1223   Ice Shelf. *Filchner-Ronne Ice Shelf Programme Report*, *8*, pp.9-11.
1224   http://nora.nerc.ac.uk/id/eprint/515954

1225

1226   Corr, H.F., Ferraccioli, F., Frearson, N., Jordan, T., Robinson, C., Armadillo, E., Caneva, G.,
1227   Bozzo, E. and Tabacco, I., 2007. Airborne radio-echo sounding of the Wilkes Subglacial Basin, the
1228   Transantarctic Mountains and the Dome C region. *TERRA ANT REPORTS*, 13, pp.55-63.
1229   https://nora.nerc.ac.uk/id/eprint/13578

1230

1231   Corr, H.F. and Vaughan, D.G., 2008. A recent volcanic eruption beneath the West Antarctic
1232   ice sheet. *NAT GEOSCI*, 1(2), pp.122-125. https://doi.org/10.1038/ngeo106

1233

1234   Creyts, T.T., Ferraccioli, F., Bell, R.E., Wolovick, M., Corr, H., Rose, K.C., Frearson, N.,
1235   Damaske, D., Jordan, T., Braaten, D. and Finn, C., 2014. Freezing of ridges and water networks
1236   preserves the Gamburtsev Subglacial Mountains for millions of years. *GEOPHYS RES LETT,* 41(22),
1237   pp.8114-8122. https://doi.org/10.1002/2014GL061491

1238

1239   Diez, A., Matsuoka, K., Ferraccioli, F., Jordan, T.A., Corr, H.F., Kohler, J., Olesen, A.V. and
1240   Forsberg, R., 2018. Basal settings control fast ice flow in the Recovery/Slessor/Bailey Region, East
1241   Antarctica. *GEOPHYS RES LETT*, 45(6), pp.2706-2715. https://doi.org/10.1002/2017GL076601

1242

1243   Diez, A., Matsuoka, K., Jordan, T.A., Kohler, J., Ferraccioli, F., Corr, H.F., Olesen, A.V.,
1244   Forsberg, R. and Casal, T.G., 2019. Patchy lakes and topographic origin for fast flow in the Recovery
1245   Glacier system, East Antarctica. *J GEOPHYS RES-EARTH*, 124(2), pp.287-304.
1246   https://doi.org/10.1029/2018JF004799

1247

1248   Drews, R., Eisen, O., Weikusat, I., Kipfstuhl, S., Lambrecht, A., Steinhage, D., Wilhelms, F.
1249   and Miller, H., 2009. Layer disturbances and the radio-echo free zone in ice sheets. *THE*
1250   *CRYOSPHERE*, 3(2), pp.195-203. https://doi.org/10.5194/tc-3-195-2009

1251

1252   EPICA Community Members, 2004. Eight glacial cycles from an Antarctic ice core.
1253   *NATURE*, 429, pp.623-628. https://doi.org/10.1038/nature02599

1254

1255   Ferraccioli, F., Gambetta, M. & Bozzo, E., 1998. Microlevelling procedures applied to
1256   regional aeromagnetic data: an example from the Transantarctic Mountains (Antarctica), *GEOPHYS*
1257   *PROSPECT*, 46, 177-196, https://doi.org/10.1046/j.1365-2478.1998.00080.x

1258

1259   Ferraccioli, F., Jones, P.C., Curtis, M.L. and Leat, P.T., 2005a. Subglacial imprints of early
1260   Gondwana break-up as identified from high resolution aerogeophysical data over western Dronning
1261   Maud Land, East Antarctica. *TERRA NOVA*, 17(6), pp.573-579. https://doi.org/10.1111/j.1365-
1262   3121.2005.00651.x

1263

1264   Ferraccioli, F., Jones, P. C., Curtis, M. L., Leat, P. T., and Riley, T. R. 2005b. Tectonic and
1265   magmatic patterns in the Jutulstraumen rift (?) region, East Antarctica, as imaged by high-resolution
1266   aeromagnetic data. *EARTH, PLANETS AND SPACE*, 57(8), pp.767-780.
1267   https://doi.org/10.1186/BF03351856

1268

1269   Ferraccioli, F., Jones, P.C., Vaughan, A.P.M. and Leat, P.T., 2006. New aerogeophysical
1270   view of the Antarctic Peninsula: More pieces, less puzzle. *GEOPHYS RES LETT*, 33(5).
1271   https://doi.org/10.1029/2005GL024636

1272

Ferraccioli, F., Jordan, T., Armadillo, E., Bozzo, E., Corr, H., Caneva, G., Robinson, C., Frearson, N. and Tabacco, I., 2007. Collaborative aerogeophysical campaign targets the Wilkes Subglacial Basin, the Transantarctic Mountains and the Dome C region. *TERRA ANT REPORTS*, *13*, pp.1-36. https://nora.nerc.ac.uk/id/eprint/13741

Ferraccioli, F., Armadillo, E., Jordan, T., Bozzo, E. and Corr, H., 2009. Aeromagnetic exploration over the East Antarctic Ice Sheet: a new view of the Wilkes Subglacial Basin. *TECTONOPHYSICS*, *478*(1-2), pp.62-77. https://doi.org/10.1016/j.tecto.2009.03.013

Ferraccioli, F., Finn, C.A., Jordan, T.A., Bell, R.E., Anderson, L.M. and Damaske, D., 2011. East Antarctic rifting triggers uplift of the Gamburtsev Mountains. *NATURE*, 479(7373), pp.388-392. https://doi.org/10.1038/nature10566

Ferris, J.K., Vaughan, A.P. and King, E.C., 2002. A window on West Antarctic crustal boundaries: the junction between the Antarctic Peninsula, the Filchner Block, and Weddell Sea oceanic lithosphere. *TECTONOPHYSICS*, 347(1-3), pp.13-23. https://doi.org/10.1016/S0040-1951(01)00235-9

Ferris, J.K., Storey, B.C., Vaughan, A.P., Kyle, P.R. and Jones, P.C., 2003. The Dufek and Forrestal intrusions, Antarctica: A centre for Ferrar large igneous province dike emplacement?. *GEOPHYS RES LETT*, 30(6). https://doi.org/10.1029/2002GL016719

Forsberg, R., Olesen, A.V., Ferraccioli, F., Jordan, T.A., Matsuoka, K., Zakrajsek, A., Ghidella, M. and Greenbaum, J.S., 2018. Exploring the Recovery Lakes region and interior Dronning Maud Land, East Antarctica, with airborne gravity, magnetic and radar measurements. *GEOLOGICAL SOCIETY, LONDON, SPECIAL PUBLICATIONS*, *461*(1), pp.23-34. https://doi.org/10.1144/SP461.17

Frederick, B.C., Young, D.A., Blankenship, D.D., Richter, T.G., Kempf, S.D., Ferraccioli, F. and Siegert, M.J., 2016. Distribution of subglacial sediments across the Wilkes Subglacial Basin, East Antarctica. *J GEOPHYS RES-EARTH*, 121(4), pp.790-813. https://doi.org/10.1002/2015JF003760

Fretwell, P., Pritchard, H.D., Vaughan, D.G., Bamber, J.L., Barrand, N.E., Bell, R., Bianchi, C., Bingham, R.G., Blankenship, D.D., Casassa, G. and Catania, G., 2013. Bedmap2: improved ice bed, surface and thickness datasets for Antarctica. *THE CRYOSPHERE*, 7(1), pp.375-393. https://doi.org/10.5194/tc-7-375-2013

Global Change Master Directory (GCMD), 2021. *GCMD Keywords, Version 12.2*. Greenbelt, MD: Earth Science Data and Information System, Earth Science Projects Division, Goddard Space Flight Center (GSFC) National Aeronautics and Space Administration (NASA). *https://forum.earthdata.nasa.gov/app.php/tag/GCMD+Keywords* [Accessed: 01/12/2021].

Golynsky, A.V., Ferraccioli, F., Hong, J.K., Golynsky, D.A., von Frese, R.R.B., Young, D.A., Blankenship, D.D., Holt, J.W., Ivanov, S.V., Kiselev, A.V. and Masolov, V.N., 2018. New magnetic anomaly map of the Antarctic. *GEOPHYS RES LETT*, *45*(13), pp.6437-6449. https://doi.org/10.1029/2018GL078153

Goodge, J.W. and Finn, C.A., 2010. Glimpses of East Antarctica: Aeromagnetic and satellite magnetic view from the central Transantarctic Mountains of East Antarctica. *J GEOPHYS RES-SOL EA*, *115*(B9). https://doi.org/10.1029/2009JB006890

Greenbaum, J.S., Blankenship, D.D., Young, D.A., Richter, T.G., Roberts, J.L., Aitken, A.R.A., Legresy, B., Schroeder, D.M., Warner, R.C., Van Ommen, T.D. and Siegert, M.J., 2015. Ocean access to a cavity beneath Totten Glacier in East Antarctica. *NAT GEOSCI*, 8(4), pp.294-298. https://doi.org/10.1038/ngeo2388

Hackney, R.I. and Featherstone, W.E., 2003. Geodetic versus geophysical perspectives of the 'gravity anomaly'. *GEOPHYS J INT*, 154(1), pp.35-43. https://doi.org/10.1046/j.1365-246X.2003.01941.x

Harlan, R.B., 1968. Eotvos corrections for airborne gravimetry. *J GEOPHYS RES*, *73*(14), pp.4675-4679. https://doi.org/10.1029/JB073i014p04675

Hélière, F., Lin, C.C., Corr, H. and Vaughan, D., 2007. Radio echo sounding of Pine Island Glacier, West Antarctica: Aperture synthesis processing and analysis of feasibility from space. *IEEE T GEOSCI REMOTE*, *45*(8), pp.2573-2582. https://doi.org/10.1109/TGRS.2007.897433

Hodgson, D.A., Jordan, T.A., Rydt, J.D., Fretwell, P.T., Seddon, S.A., Becker, D., Hogan, K.A., Smith, A.M. and Vaughan, D.G., 2019. Past and future dynamics of the Brunt Ice Shelf from seabed bathymetry and ice shelf geometry. *THE CRYOSPHERE*, *13*(2), pp.545-556. https://doi.org/10.5194/tc-13-545-2019

Hofstede, C., Beyer, S., Corr, H., Eisen, O., Hattermann, T., Helm, V., Neckel, N., Smith, E.C., Steinhage, D., Zeising, O. and Humbert, A., 2021. Evidence for a grounding line fan at the onset of a basal channel under the ice shelf of Support Force Glacier, Antarctica, revealed by reflection seismics. *THE CRYOSPHERE*, *15*(3), pp.1517-1535. https://doi.org/10.5194/tc-15-1517-2021

Hogan, K.A., Larter, R.D., Graham, A.G., Arthern, R., Kirkham, J.D., Totten Minzoni, R., Jordan, T.A., Clark, R., Fitzgerald, V., Wåhlin, A.K. and Anderson, J.B., 2020. Revealing the former bed of Thwaites Glacier using sea-floor bathymetry: implications for warm-water routing and bed

controls on ice flow and buttressing. *THE CRYOSPHERE*, *14*(9), pp.2883-2908. https://doi.org/10.5194/tc-14-2883-2020

Holland, P.R., Corr, H.F., Vaughan, D.G., Jenkins, A. and Skvarca, P., 2009. Marine ice in Larsen ice shelf. *GEOPHYS RES LETT*, *36*(11). https://doi.org/10.1029/2009GL038162

Holland, P.R., Corr, H.F., Pritchard, H.D., Vaughan, D.G., Arthern, R.J., Jenkins, A. and Tedesco, M., 2011. The air content of Larsen ice shelf. *GEOPHYS RES LETT*, *38*(10). https://doi.org/10.1029/2011GL047245

Holschuh, N., Christianson, K., Paden, J., Alley, R.B. and Anandakrishnan, S., 2020. Linking postglacial landscapes to glacier dynamics using swath radar at Thwaites Glacier, Antarctica. *GEOLOGY*, *48*(3), pp.268-272. https://doi.org/10.1130/G46772.1

Holt, J.W., Blankenship, D.D., Morse, D.L., Young, D.A., Peters, M.E., Kempf, S.D., Richter, T.G., Vaughan, D.G. and Corr, H.F., 2006. New boundary conditions for the West Antarctic Ice Sheet: Subglacial topography of the Thwaites and Smith glacier catchments. *GEOPHYS RES LETT*, *33*(9). https://doi.org/10.1029/2005GL025561

Howat, I.M., Porter, C., Smith, B.E., Noh, M.J. and Morin, P., 2019. The reference elevation model of Antarctica. *THE CRYOSPHERE*, *13*(2), pp.665-674. https://doi.org/10.5194/tc-13-665-2019

IPCC, 2021: Climate Change 2021: The Physical Science Basis. Contribution of Working Group I to the Sixth Assessment Report of the Intergovernmental Panel on Climate Change [Masson-Delmotte, V., P. Zhai, A. Pirani, S.L. Connors, C. Péan, S. Berger, N. Caud, Y. Chen, L. Goldfarb, M.I. Gomis, M. Huang, K. Leitzell, E. Lonnoy, J.B.R. Matthews, T.K. Maycock, T. Waterfield, O. Yelekçi, R. Yu, and B. Zhou (eds.)]. Cambridge University Press. In Press.

Jeofry, H., Ross, N., Corr, H.F., Li, J., Morlighem, M., Gogineni, P. and Siegert, M.J., 2018. A new bed elevation model for the Weddell Sea sector of the West Antarctic Ice Sheet. *EARTH SYST SCI DATA*, 10(2), pp.711-725. https://doi.org/10.5194/essd-10-711-2018

Johnson, A., Cheeseman, S. and Ferris, J., 1999. Improved compilation of Antarctic Peninsula magnetic data by new interactive grid suturing and blending methods. *ANN GEOPHYS-ITALY*, 42(2). https://doi.org/10.4401/ag-3717

Jones, P.C., Johnson, A.C., von Frese, R.R. and Corr, H., 2002. Detecting rift basins in the Evans Ice Stream region of West Antarctica using airborne gravity data. *TECTONOPHYSICS*, 347(1-3), pp.25-41. https://doi.org/10.1016/S0040-1951(01)00236-0

1392

1393   Jordan, T., Ferraccioli, F., Corr, H., Robinson, C., Caneva, G., Armadillo, E., Bozzo, E. and
1394   Frearson, N., 2007. Linking the Wilkes Subglacial Basin the Transantarctic Mountains and the Ross
1395   Sea with a new airborne gravity survey. *TERRA ANT REPORTS*, *13*, pp.37-54.
1396   https://nora.nerc.ac.uk/id/eprint/15749

1397

1398   Jordan, T.A., Ferraccioli, F., Jones, P.C., Smellie, J.L., Ghidella, M. and Corr, H., 2009.
1399   Airborne gravity reveals interior of Antarctic volcano. *PHYS EARTH PLANET IN*, 175(3-4), pp.127-
1400   136. https://doi.org/10.1016/j.pepi.2009.03.004

1401

1402   Jordan, T. A., Ferraccioli, F., Vaughan, D. G., Holt, J. W., Corr, H., Blankenship, D. D., &
1403   Diehl, T. M. (2010). Aerogravity evidence for major crustal thinning under the Pine Island Glacier
1404   region (West Antarctica). *BULLETIN*, *122*(5-6), 714-726. https://doi.org/10.1130/B26417.1

1405

1406   Jordan, T.A., Ferraccioli, F., Armadillo, E. and Bozzo, E., 2013. Crustal architecture of the
1407   Wilkes Subglacial Basin in East Antarctica, as revealed from airborne gravity data.
1408   *TECTONOPHYSICS*, 585, pp.196-206. https://doi.org/10.1016/j.tecto.2012.06.041

1409

1410   Jordan, T.A., Neale, R.F., Leat, P.T., Vaughan, A.P.M., Flowerdew, M.J., Riley, T.R.,
1411   Whitehouse, M.J. and Ferraccioli, F., 2014. Structure and evolution of Cenozoic arc magmatism on
1412   the Antarctic Peninsula: a high resolution aeromagnetic perspective. *GEOPHYS J INT*, *198*(3),
1413   pp.1758-1774. https://doi.org/10.1093/gji/ggu233

1414

1415   Jordan, T.A., Martin, C., Ferraccioli, F., Matsuoka, K., Corr, H., Forsberg, R., Olesen, A. and
1416   Siegert, M., 2018. Anomalously high geothermal flux near the South Pole. *SCI REP-UK*, *8*(1), pp.1-8.
1417   https://doi.org/10.1038/s41598-018-35182-0

1418

1419   Jordan, T.A. and Becker, D., 2018. Investigating the distribution of magmatism at the onset of
1420   Gondwana breakup with novel strapdown gravity and aeromagnetic data. *PHYS EARTH PLANET IN*,
1421   *282*, pp.77-88. https://doi.org/10.1016/j.pepi.2018.07.007

1422

1423   Jordan, T.A., Porter, D., Tinto, K., Millan, R., Muto, A., Hogan, K., Larter, R.D., Graham,
1424   A.G. and Paden, J.D., 2020. New gravity-derived bathymetry for the Thwaites, Crosson, and Dotson
1425   ice shelves revealing two ice shelf populations. *THE CRYOSPHERE*, *14*(9), pp.2869-2882.
1426   https://doi.org/10.5194/tc-14-2869-2020

1427

1428   Karlsson, N.B., Rippin, D.M., Vaughan, D.G. and Corr, H.F., 2009. The internal layering of
1429   Pine Island Glacier, West Antarctica, from airborne radar-sounding data. *ANN GLACIOL*, 50(51),
1430   pp.141-146. https://doi.org/3189/S0260305500250660

1431

1432   Karlsson, N.B., Rippin, D.M., Bingham, R.G. and Vaughan, D.G., 2012. A 'continuity-index'
1433 for assessing ice-sheet dynamics from radar-sounded internal layers. *EARTH PLANET SC LETT*, 335,
1434 pp.88-94. https://doi.org/10.1016/j.epsl.2012.04.034

1435

1436   Karlsson, N.B., Bingham, R.G., Rippin, D.M., Hindmarsh, R.C., Corr, H.F. and Vaughan,
1437 D.G., 2014. Constraining past accumulation in the central Pine Island Glacier basin, West Antarctica,
1438 using radio-echo sounding. *J GLACIOL*, 60(221), pp.553-562.
1439 https://doi.org/10.3189/2014JoG13j180

1440

1441   Karlsson, N.B., Binder, T., Eagles, G., Helm, V., Pattyn, F., Liefferinge, B.V. and Eisen, O.,
1442 2018. Glaciological characteristics in the Dome Fuji region and new assessment for "Oldest Ice".
1443 *THE CRYOSPHERE*, *12*(7), pp.2413-2424. https://doi.org/10.5194/tc-12-2413-2018

1444

1445   Lei, Y., Gardner, A.S. and Agram, P., 2021. Processing methodology for the ITS_LIVE
1446 Sentinel-1 ice velocity product. *EARTH SYST SCI DATA DISCUSSIONS*, pp.1-27.
1447 https://doi.org/10.5194/essd-2021-393

1448

1449   Le Brocq, A.M., Payne, A.J. and Vieli, A., 2010. An improved Antarctic dataset for high
1450 resolution numerical ice sheet models (ALBMAP v1). *EARTH SYST SCI DATA*, 2(2), pp.247-260.
1451 https://doi.org/10.5194/essd-2-247-2010

1452

1453   Le Brocq, A.M., Ross, N., Griggs, J.A., Bingham, R.G., Corr, H.F., Ferraccioli, F., Jenkins,
1454 A., Jordan, T.A., Payne, A.J., Rippin, D.M. and Siegert, M.J., 2013. Evidence from ice shelves for
1455 channelized meltwater flow beneath the Antarctic Ice Sheet. *NAT GEOSCI*, 6(11), pp.945-948.
1456 https://doi.org/10.1038/ngeo1977

1457

1458   Luo, K., Liu, S., Guo, J., Wang, T., Li, L., Cui, X., Sun, B. and Tang, X., 2020. Radar-
1459 Derived Internal Structure and Basal Roughness Characterization along a Traverse from Zhongshan
1460 Station to Dome A, East Antarctica. *REMOTE SENSING*, 12(7), p.1079.
1461 https://doi.org/10.3390/rs12071079

1462

1463   Lythe, M.B. and Vaughan, D.G., 2001. BEDMAP: A new ice thickness and subglacial
1464 topographic model of Antarctica. *J GEOPHYS RES-SOL EA*, *106*(B6), pp.11335-11351.
1465 https://doi.org/10.1029/2000JB900449

1466

1467   MacGregor, J.A., Boisvert, L.N., Medley, B., Petty, A.A., Harbeck, J.P., Bell, R.E., Blair,
1468 J.B., Blanchard-Wrigglesworth, E., Buckley, E.M., Christoffersen, M.S. and Cochran, J.R., 2021. The
1469 scientific legacy of NASA's Operation Icebridge. *REV GEOPHYS*, *59*(2).
1470 https://doi.org/10.1029/2020RG000712

1471

1472   Millan, R., Rignot, E., Bernier, V., Morlighem, M. and Dutrieux, P., 2017. Bathymetry of the
1473   Amundsen Sea Embayment sector of West Antarctica from Operation IceBridge gravity and other
1474   data. *GEOPHYS RES LETT*, *44*(3), pp.1360-1368. https://doi.org/10.1002/2016GL072071

1475

1476   Moritz, H., 1980. Geodetic reference system 1980. *B GEOD*, *54*(3), pp.395-405.
1477   https://doi.org/10.1007/s001900050278

1478

1479   Morlighem, M., C. Williams, E. Rignot, L. An, J. E. Arndt, J. Bamber, G. Catania, N.
1480   Chauché, J. A. Dowdeswell, B. Dorschel, I. Fenty, K. Hogan, I. Howat, A. Hubbard, M. Jakobsson, T.
1481   M. Jordan, K. K. Kjeldsen, R. Millan, L. Mayer, J. Mouginot, B. Noël, C. O'Cofaigh, S. J. Palmer, S.
1482   Rysgaard, H. Seroussi, M. J. Siegert, P. Slabon, F. Straneo, M. R. van den Broeke, W. Weinrebe, M.
1483   Wood, and K. Zinglersen. 2017. BedMachine v3: Complete bed topography and ocean bathymetry
1484   mapping of Greenland from multi-beam echo sounding combined with mass conservation. *GEOPHYS
1485   RES LETT*, 44. https://doi.org/10.1002/2017GL074954

1486

1487   Morlighem, M. 2020. *MEaSUREs BedMachine Antarctica, Version 2*. Boulder, Colorado
1488   USA. NASA National Snow and Ice Data Center Distributed Active Archive Center. doi:
1489   https://doi.org/10.5067/E1QL9HFQ7A8M.

1490

1491   Morlighem, M., Rignot, E., Binder, T., Blankenship, D., Drews, R., Eagles, G., Eisen, O.,
1492   Ferraccioli, F., Forsberg, R., Fretwell, P. and Goel, V., 2020. Deep glacial troughs and stabilizing
1493   ridges unveiled beneath the margins of the Antarctic ice sheet. *NAT GEOSCI*, 13(2), pp.132-137.
1494   https://doi.org/10.1038/s41561-019-0510-8

1495

1496   Napoleoni, F., Jamieson, S.S., Ross, N., Bentley, M.J., Rivera, A., Smith, A.M., Siegert, M.J.,
1497   Paxman, G.J., Gacitúa, G., Uribe, J.A. and Zamora, R., 2020. Subglacial lakes and hydrology across
1498   the Ellsworth Subglacial Highlands, West Antarctica. *THE CRYOSPHERE*, 14(12), pp.4507-4524.
1499   https://doi.org/10.5194/tc-14-4507-2020

1500

1501   Paden, J., J. Li, C. Leuschen, F. Rodriguez-Morales, and R. Hale. 2014, updated 2021.
1502   *IceBridge MCoRDS L1B Geolocated Radar Echo Strength Profiles, Version 2*. Boulder, Colorado
1503   USA. NASA National Snow and Ice Data Center Distributed Active Archive Center.
1504   https://doi.org/10.5067/90S1XZRBAX5N [Accessed: 01/12/2021].

1505

1506   Parrenin, F., Hindmarsh, R., 2007. Influence of a non-uniform velocity field on isochrone
1507   geometry along a steady flowline of an ice sheet. *J GLACIOL*, 53(183), 612-622.
1508   https://doi.org/10.3189/002214307784409298.

1509

1510   Paxman, G.J., Jamieson, S.S., Ferraccioli, F., Jordan, T.A., Bentley, M.J., Ross, N., Forsberg,
1511   R., Matsuoka, K., Steinhage, D., Eagles, G. and Casal, T.G., 2019. Subglacial Geology and

Geomorphology of the Pensacola-Pole Basin, East Antarctica. *GEOCHEMISTRY, GEOPHYSICS, GEOSYSTEMS*, *20*(6), pp.2786-2807. https://doi.org/10.1029/2018GC008126

Peters, M.E., Blankenship, D.D. and Morse, D.L., 2005. Analysis techniques for coherent airborne radar sounding: Application to West Antarctic ice streams. *J GEOPHYS RES-SOL EA, 110*(B6). https://doi.org/10.1029/2004JB003222

Peters, M.E., Blankenship, D.D., Carter, S.P., Kempf, S.D., Young, D.A. and Holt, J.W., 2007. Along-track focusing of airborne radar sounding data from West Antarctica for improving basal reflection analysis and layer detection. *IEEE T GEOSCI REMOTE*, 45(9), pp.2725-2736. https://doi.org/10.1109/TGRS.2007.897416

Rignot, E., Mouginot, J., & Scheuchl, B. (2017). *MEaSUREs InSAR-based Antarctica ice velocity map, version 2*. NASA National Snow and Ice Data Center Distributed Active Archive Center. https://doi.org/10.5067/D7GK8F5J8M8R

Rippin, D.M., Bamber, J.L., Siegert, M.J., Vaughan, D.G. and Corr, H.F.J., 2003a. Basal topography and ice flow in the Bailey/Slessor region of East Antarctica. *J GEOPHYS RES-EARTH*, 108(F1). https://doi.org/10.1029/2003JF000039

Rippin, D.M., Siegert, M.J. and Bamber, J.L., 2003b. The englacial stratigraphy of Wilkes Land, East Antarctica, as revealed by internal radio-echo sounding layering, and its relationship with balance velocities. *ANN GLACIOL*, *36*, pp.189-196. https://doi.org/10.3189/172756403781816356

Rippin, D.M., Bamber, J.L., Siegert, M.J., Vaughan, D.G. and Corr, H.F.J., 2006. Basal conditions beneath enhanced-flow tributaries of Slessor Glacier, East Antarctica. *J GLACIOL*, *52*(179), pp.481-490. https://doi.org/10.3189/172756506781828467

Rippin, D.M., Vaughan, D.G. and Corr, H.F., 2011. The basal roughness of Pine Island Glacier, West Antarctica. *J GLACIOL*, *57*(201), pp.67-76. https://doi.org/10.3189/002214311795306574

Rippin, D.M., Bingham, R.G., Jordan, T.A., Wright, A.P., Ross, N., Corr, H.F., Ferraccioli, F., Le Brocq, A.M., Rose, K.C. and Siegert, M.J., 2014. Basal roughness of the Institute and Möller Ice Streams, West Antarctica: Process determination and landscape interpretation. *GEOMORPHOLOGY*, *214*, pp.139-147. https://doi.org/10.1016/j.geomorph.2014.01.021

Robin, G.D.Q., Swithinbank, C.W.M. and Smith, B.M.E., 1970. Radio echo exploration of the Antarctic ice sheet. *INTERNATIONAL ASSOCIATION OF SCIENTIFIC HYDROLOGY PUBLICATION*, *86*, pp.97-115.

1552

Robin, G.D.Q., Drewry, D.J. and Meldrum, D.T., 1977. International studies of ice sheet and bedrock. *PHILOS T ROY SOC B*, *279*(963), pp.185-196. https://doi.org/10.1098/rstb.1977.0081

1555

Rose, K.C., Ferraccioli, F., Jamieson, S.S., Bell, R.E., Corr, H., Creyts, T.T., Braaten, D., Jordan, T.A., Fretwell, P.T. and Damaske, D., 2013. Early east Antarctic Ice Sheet growth recorded in the landscape of the Gamburtsev Subglacial Mountains. *EARTH PLANET SC LETT*, 375, pp.1-12. https://doi.org/10.1016/j.epsl.2013.03.053

1560

Rose, K.C., Ross, N., Bingham, R.G., Corr, H.F., Ferraccioli, F., Jordan, T.A., Le Brocq, A.M., Rippin, D.M. and Siegert, M.J., 2014. A temperate former West Antarctic ice sheet suggested by an extensive zone of subglacial meltwater channels. *GEOLOGY*, *42*(11), pp.971-974. https://doi.org/10.1130/G35980.1

1565

Ross, N., Bingham, R.G., Corr, H.F., Ferraccioli, F., Jordan, T.A., Le Brocq, A., Rippin, D.M., Young, D., Blankenship, D.D. and Siegert, M.J., 2012. Steep reverse bed slope at the grounding line of the Weddell Sea sector in West Antarctica. *NAT GEOSCI*, *5*(6), pp.393-396. https://doi.org/10.1038/ngeo1468

1570

Ross, N., Jordan, T.A., Bingham, R.G., Corr, H.F., Ferraccioli, F., Le Brocq, A., Rippin, D.M., Wright, A.P. and Siegert, M.J., 2014. The Ellsworth subglacial highlands: inception and retreat of the West Antarctic Ice Sheet. *BULLETIN*, *126*(1-2), pp.3-15. https://doi.org/10.1130/B30794.1

1574

Ross, N., Corr, H. and Siegert, M., 2020. Large-scale englacial folding and deep-ice stratigraphy within the West Antarctic Ice Sheet. *THE CRYOSPHERE,* 14(6), pp.2103-2114. https://doi.org/10.5194/tc-14-2103-2020

1578

Scheinert, M., Ferraccioli, F., Schwabe, J., Bell, R., Studinger, M., Damaske, D., ... & Richter, T. D. (2016). New Antarctic gravity anomaly grid for enhanced geodetic and geophysical studies in Antarctica. *GEOPHYS RES LETT*, 43(2), 600-610. https://doi.org/10.1002/2015GL067439

1582

Schroeder, D.M., Blankenship, D.D. and Young, D.A., 2013. Evidence for a water system transition beneath Thwaites Glacier, West Antarctica. *P NATL A SCI*, *110*(30), pp.12225-12228. https://doi.org/10.1073/pnas.1302828110

1586

Schroeder, D.M., Blankenship, D.D., Young, D.A. and Quartini, E., 2014. Evidence for elevated and spatially variable geothermal flux beneath the West Antarctic Ice Sheet. *P NATL A SCI*, *111*(25), pp.9070-9072. https://doi.org/10.1073/pnas.1405184111

1590

1591 Schroeder, D.M., Dowdeswell, J.A., Siegert, M.J., Bingham, R.G., Chu, W., MacKie, E.J.,
1592 Siegfried, M.R., Vega, K.I., Emmons, J.R. and Winstein, K., 2019. Multidecadal observations of the
1593 Antarctic ice sheet from restored analog radar records. *P NATL A SCI*, *116*(38), pp.18867-18873.
1594 https://doi.org/10.1073/pnas.1821646116

1595

1596 Shepherd, T., Bamber, J.L. and Ferraccioli, F., 2006. Subglacial geology in Coats Land, East
1597 Antarctica, revealed by airborne magnetics and radar sounding. *EARTH PLANET SC LETT*, 244(1-2),
1598 pp.323-335. https://doi.org/10.1016/j.epsl.2006.01.068

1599

1600 Siegert, M.J., Payne, A.J. and Joughin, I., 2003. Spatial stability of Ice Stream D and its
1601 tributaries, West Antarctica, revealed by radio-echo sounding and interferometry. *ANN GLACIOL*, *37*,
1602 pp.377-382. https://doi.org/10.3189/172756403781816022

1603

1604 Siegert, M.J. and Payne, A.J., 2004. Past rates of accumulation in central West Antarctica.
1605 *GEOPHYS RES LETT*, 31(12). https://doi.org/10.1029/2004GL020290

1606

1607 Siegert, M., Ross, N., Corr, H., Kingslake, J. and Hindmarsh, R., 2013. Late Holocene ice-
1608 flow reconfiguration in the Weddell Sea sector of West Antarctica. *QUATERNARY SCI REV*, *78*,
1609 pp.98-107. https://doi.org/10.1016/j.quascirev.2013.08.003

1610

1611 Siegert, M.J., Ross, N., Corr, H., Smith, B., Jordan, T., Bingham, R.G., Ferraccioli, F.,
1612 Rippin, D.M. and Le Brocq, A., 2014. Boundary conditions of an active West Antarctic subglacial
1613 lake: implications for storage of water beneath the ice sheet. *THE CRYOSPHERE*, *8*(1), pp.15-24.
1614 https://doi.org/10.5194/tc-8-15-2014

1615

1616 Sigl, M., Fudge, T.J., Winstrup, M., Cole-Dai, J., Ferris, D., McConnell, J.R., Taylor, K.C.,
1617 Welten, K.C., Woodruff, T.E., Adolphi, F. and Bisiaux, M., 2016. The WAIS Divide deep ice core
1618 WD2014 chronology–Part 2: Annual-layer counting (0–31 ka BP). *CLIM PAST*, *12*(3), pp.769-786.
1619 https://doi.org/10.5194/cp-12-769-2016

1620

1621 Studinger, M., Bell, R.E., Blankenship, D.D., Finn, C.A., Arko, R.A., Morse, D.L. and
1622 Joughin, I., 2001. Subglacial sediments: A regional geological template for ice flow in West
1623 Antarctica. *GEOPHYS RES LETT*, *28*(18), pp.3493-3496. https://doi.org/10.1029/2000GL011788

1624

1625 Sutter, J., Fischer, H. and Eisen, O., 2021. Investigating the internal structure of the Antarctic
1626 ice sheet: the utility of isochrones for spatiotemporal ice-sheet model calibration. *THE
1627 CRYOSPHERE*, 15, 3839-3860. https://doi.org/10.5194/tc-15-3839-2021

1628

1629   Tinto, K.J. and Bell, R.E., 2011. Progressive unpinning of Thwaites Glacier from newly identified
1630   offshore ridge: Constraints from aerogravity. *GEOPHYS RES LETT*, 38(20).
1631   https://doi.org/10.1029/2011GL049026

1632

1633   Tinto, K.J., Padman, L., Siddoway, C.S., Springer, S.R., Fricker, H.A., Das, I., Tontini, F.C.,
1634   Porter, D.F., Frearson, N.P., Howard, S.L. and Siegfried, M.R., 2019. Ross Ice Shelf response to
1635   climate driven by the tectonic imprint on seafloor bathymetry. *NAT GEOSCI*, *12*(6), pp.441-449.
1636   https://doi.org/10.1038/s41561-019-0370-2

1637

1638   Valliant, H.D., 1992. LaCoste & Romberg Air/Sea Meters: An Overview, CRC Handbook of
1639   Geophysical Exploration at Sea. London, CRC Press.

1640

1641   Vaughan, D.G., Corr, H.F., Ferraccioli, F., Frearson, N., O'Hare, A., Mach, D., Holt, J.W.,
1642   Blankenship, D.D., Morse, D.L. and Young, D.A., 2006. New boundary conditions for the West
1643   Antarctic ice sheet: Subglacial topography beneath Pine Island Glacier. *GEOPHYS RES LETT*, 33(9).
1644   https://doi.org/10.1029/2005GL025588

1645

1646   Vaughan, D.G., Corr, H.F., Smith, A.M., Pritchard, H.D. and Shepherd, A., 2008. Flow-
1647   switching and water piracy between Rutford ice stream and Carlson inlet, West Antarctica. *Journal of*
1648   *Glaciology*, 54(184), pp.41-48. https://doi.org/10.3189/002214308784409125

1649

1650   Vaughan, D.G., Corr, H.F., Bindschadler, R.A., Dutrieux, P., Gudmundsson, G.H., Jenkins,
1651   A., Newman, T., Vornberger, P. and Wingham, D.J., 2012. Subglacial melt channels and fracture in
1652   the floating part of Pine Island Glacier, Antarctica. *J GEOPHYS RES-EARTH*, *117*(F3).
1653   https://doi.org/10.1029/2012JF002360

1654

1655   Wilkinson, M.D., Dumontier, M., Aalbersberg, I.J., Appleton, G., Axton, M., Baak, A.,
1656   Blomberg, N., Boiten, J.W., da Silva Santos, L.B., Bourne, P.E. and Bouwman, J., 2016. The FAIR
1657   Guiding Principles for scientific data management and stewardship. *SCI. DATA*, *3*(1), pp.1-9.
1658   https://doi.org/10.1038/sdata.2016.18

1659

1660   Winski, D.A., Fudge, T.J., Ferris, D.G., Osterberg, E.C., Fegyveresi, J.M., Cole-Dai, J.,
1661   Thundercloud, Z., Cox, T.S., Kreutz, K.J., Ortman, N. and Buizert, C., 2019. The SP19 chronology
1662   for the South Pole Ice Core–Part 1: volcanic matching and annual layer counting. *CLIM PAST*, 15(5),
1663   pp.1793-1808. https://doi.org/10.5194/cp-15-1793-2019

1664
1665   Winter, K., Woodward, J., Ross, N., Dunning, S.A., Bingham, R.G., Corr, H.F. and Siegert,
1666   M.J., 2015. Airborne radar evidence for tributary flow switching in Institute Ice Stream, West
1667   Antarctica: Implications for ice sheet configuration and dynamics. *J GEOPHYS RES-EARTH*, *120*(9),
1668   pp.1611-1625. https://doi.org/10.1002/2015JF003518
1669

Winter, K., Ross, N., Ferraccioli, F., Jordan, T.A., Corr, H.F., Forsberg, R., Matsuoka, K., Olesen, A.V. and Casal, T.G., 2018. Topographic steering of enhanced ice flow at the bottleneck between East and West Antarctica. *GEOPHYS RES LETT*, *45*(10), pp.4899-4907. https://doi.org/10.1029/2018GL077504

Wright, A.P., Young, D.A., Roberts, J.L., Schroeder, D.M., Bamber, J.L., Dowdeswell, J.A., Young, N.W., Le Brocq, A.M., Warner, R.C., Payne, A.J. and Blankenship, D.D., 2012. Evidence of a hydrological connection between the ice divide and ice sheet margin in the Aurora Subglacial Basin, East Antarctica. *J GEOPHYS RES-EARTH*, *117*(F1). https://doi.org/10.1029/2011JF002066

Young, D.A., Schroeder, D.M., Blankenship, D.D., Kempf, S.D. and Quartini, E., 2016. The distribution of basal water between Antarctic subglacial lakes from radar sounding. *PHILOS T R SOC A*, *374*(2059), p.20140297. https://doi.org/10.1098/rsta.2014.0297

Young, T.J., Schroeder, D.M., Jordan, T.M., Christoffersen, P., Tulaczyk, S.M., Culberg, R. and Bienert, N.L., 2021. Inferring ice fabric from birefringence loss in airborne radargrams: Application to the eastern shear margin of Thwaites Glacier, West Antarctica. *J GEOPHYS RES-EARTH*, *126*(5), p.e2020JF006023. https://doi.org/10.1029/2020JF006023